

**DAHLGREN DIVISION
NAVAL SURFACE WARFARE CENTER**

Dahlgren, Virginia 22448-5100



NSWCDD/TR-96/133

**NONLINEAR STRUCTURAL LOAD DISTRIBUTION
METHODOLOGY FOR THE AEROPREDICTION CODE**

BY ROY M. MCINVILLE FRANK G. MOORE

WEAPONS SYSTEMS DEPARTMENT

CLINT HOUSH

NAVAL AIR WARFARE CENTER

WEAPONS DIVISION, CHINA LAKE

SEPTEMBER 1996

19961125 124

Approved for public release; distribution is unlimited.

REPORT DOCUMENTATION PAGE			Form Approved OMB No. 0704-0188	
Public reporting burden for this collection of information is estimated to average 1 hour per response, including the time for reviewing instructions, search existing data sources, gathering and maintaining the data needed, and completing and reviewing the collection of information. Send comments regarding this burden or any other aspect of this collection of information, including suggestions for reducing this burden, to Washington Headquarters Services, Directorate for Information Operations and Reports, 1215 Jefferson Davis Highway, Suite 1204, Arlington, VA 22202-4302, and to the Office of Management and Budget, Paperwork Reduction Project (0704-0188), Washington, DC 20503.				
1. AGENCY USE ONLY (Leave blank)		2. REPORT DATE September 1996		3. REPORT TYPE AND DATES COVERED Draft
4. TITLE AND SUBTITLE Nonlinear Structural Load Distribution Methodology for the Aeroprediction Code			5. FUNDING NUMBERS	
6. AUTHOR(s) Roy M. McInville, Frank G. Moore, Clint Housh				
7. PERFORMING ORGANIZATION NAME(S) AND ADDRESS(ES) Commander Naval Surface Warfare Center Dahlgren Division (Code G04) 17320 Dahlgren Road Dahlgren, VA 22448-5100			8. PERFORMING ORGANIZATION REPORT NUMBER NSWCDD/TR-96/133	
9. SPONSORING/MONITORING AGENCY NAME(S) AND ADDRESS(ES)			10. SPONSORING/MONITORING AGENCY REPORT NUMBER	
11. SUPPLEMENTARY NOTES				
12a. DISTRIBUTION/AVAILABILITY STATEMENT Approved for public release; distribution is unlimited.			12b. DISTRIBUTION CODE	
13. ABSTRACT (Maximum 200 words) New methodology has been added to the NSWCDD Aeroprediction code to permit the distribution of the local linear and nonlinear aerodynamic loads along the body length and over the wing and tail lifting surfaces. The new techniques extend to both the $\Phi = 0$ deg and $\Phi = 45$ deg roll positions and to both windward and leeward lifting surfaces in the 45 deg orientation. The local loads are integrated to get the distribution of the shear and bending moments for use in structural analysis and design. Navier-Stokes CFD computations for the Seasparrow missile were used in the development of these extensions to the code and in validating their effectiveness. In general, good agreement with the CFD results is obtained.				
14. SUBJECT TERMS Aeroprediction Code, AP95, wing-body-tail configuration, body loading, linear load, non-linear load, normal force, wing-alone normal force, bending moment, wing deflection			15. NUMBER OF PAGES 83	
			16. PRICE CODE	
17. SECURITY CLASSIFICATION OF REPORTS UNCLASSIFIED	18. SECURITY CLASSIFICATION OF THIS PAGE UNCLASSIFIED	19. SECURITY CLASSIFICATION OF ABSTRACT UNCLASSIFIED	20. LIMITATION OF ABSTRACT UL	

FOREWORD

The latest version of the NSWCDD Aeroprediction code (AP95) produces linear aerodynamic loads that are based on theoretical methods which compute pressures all along the body and lifting surfaces. These linear loads can be integrated to obtain total shear and bending moments for use in structural design and analysis. The AP95 also computes the total nonlinear aerodynamic loads but not in pressure distribution form. Thus, the nonlinear term of the aerodynamic load (which is quite large at high angle of attack) is not included in the shear and bending moment calculations. As a result, the AP95 is not as useful to the structural design engineer as it could be. To remedy this situation, new technology was developed to distribute these nonlinear loads on the various missile or projectile components. This new technology is discussed in this report.

The work described in this report was supported through the Office of Naval Research (Mr. Dave Siegel) by the following programs: the Air Launched Weapons Program managed at the Naval Air Warfare Center, China Lake, CA, by Mr. Tom Loftus and Dr. Craig Porter, and the Surface Weapons Systems Technology Program managed at the Naval Surface Warfare Center, Dahlgren Division (NSWCDD) by Mr. Robin Staton and Mr. Gil Graff. Also, some support was provided by the Marine Corps Weaponry Technology Program managed at NSWCDD by Mr. Bob Stiegler. The authors express appreciation for support received in this work.

Approved by:



DAVID S. MALYEVAC, Deputy Head
Weapons Systems Department

CONTENTS

<u>Section</u>	<u>Page</u>
1.0 INTRODUCTION.....	1
2.0 ANALYSIS.....	1
2.1 BODY LOADS AT THE $\Phi = 0$ DEG ROLL POSITION	2
2.2 LIFTING SURFACE LOADS AT THE $\Phi = 0$ DEG ROLL POSITION.....	6
2.3 CHANGES FOR THE $\Phi = 45$ DEG ROLL POSITION.....	10
2.4 LOADS, SHEAR, AND BENDING MOMENTS	14
3.0 RESULTS AND DISCUSSION	15
3.1 CFD METHODOLOGY	15
3.2 RESULTS FOR $\Phi = 0$ DEG ROLL POSITION	18
3.3 RESULTS FOR $\Phi = 45$ DEG ROLL POSITION	19
3.4 RESULTS FOR WING DEFLECTION.....	20
4.0 SUMMARY	20
5.0 REFERENCES	22
6.0 SYMBOLS AND DEFINITIONS	24
DISTRIBUTION.....	(1)

ILLUSTRATIONS

<u>Figure</u>		<u>Page</u>
1	EFFECT OF ADJUSTMENT OF NONLINEAR COMPONENT OF NOSE LOAD	31
2	DISTRIBUTION OF UNIFORM BODY-WING INTERFERENCE LOADS.....	32
3	DISTRIBUTION OF TRAPEZOIDAL BODY-WING INTERFERENCE LOADS	33
4	GEOMETRY OF WING-TAIL INTERFERENCE DISTRIBUTION MODEL.....	34
5	DISTRIBUTION OF NEGATIVE COMPONENT OF BODY- WING INTERFERENCE LOADS.....	35
6	SEASPARROW MISSILE	36
7	BODY LOADING AT $\Phi = 0^\circ$: (a) ALPHA = 10° , (b) ALPHA = 25° , AND (c) ALPHA = 40°	37
8	BODY SHEAR AT $\Phi = 0^\circ$: (a) ALPHA = 10° , (b) ALPHA = 25° , AND (c) ALPHA = 40°	38
9	BODY BENDING MOMENT AT $\Phi = 0^\circ$: (a) ALPHA = 10° , (b) ALPHA = 25° , AND (c) ALPHA = 40°	39
10	WING LOADING AT $\Phi = 0^\circ$: (a) ALPHA = 10° , (b) ALPHA = 25° , AND (c) ALPHA = 40°	40
11	WING SHEAR AT $\Phi = 0^\circ$: (a) ALPHA = 10° , (b) ALPHA = 25° , AND (c) ALPHA = 40°	41
12	WING BENDING MOMENT AT $\Phi = 0^\circ$: (a) ALPHA = 10° , (b) ALPHA = 25° , AND (c) ALPHA = 40°	42
13	TAIL LOADING AT $\Phi = 0^\circ$: (a) ALPHA = 10° , (b) ALPHA = 25° , AND (c) ALPHA = 40°	43

ILLUSTRATIONS (Continued)

<u>Figure</u>		<u>Page</u>
14	TAIL SHEAR AT $\Phi = 0^\circ$: (a) ALPHA = 10° , (b) ALPHA = 25° , AND (c) ALPHA = 40°	44
15	TAIL BENDING MOMENT AT $\Phi = 0^\circ$: (a) ALPHA = 10° , (b) ALPHA = 25° , AND (c) ALPHA = 40°	45
16	BODY LOADING AT $\Phi = 45^\circ$: (a) ALPHA = 10° , (b) ALPHA = 25° , AND (c) ALPHA = 40°	46
17	BODY SHEAR AT $\Phi = 45^\circ$: (a) ALPHA = 10° , (b) ALPHA = 25° , AND (c) ALPHA = 40°	47
18	BODY BENDING MOMENT AT $\Phi = 45^\circ$: (a) ALPHA = 10° , (b) ALPHA = 25° , AND (c) ALPHA = 40°	48
19	WINDWARD WING LOADING AT $\Phi = 45^\circ$: (a) ALPHA = 10° , (b) ALPHA = 25° , AND (c) ALPHA = 40°	49
20	WINDWARD WING SHEAR AT $\Phi = 45^\circ$: (a) ALPHA = 10° , (b) ALPHA = 25° , AND (c) ALPHA = 40°	50
21	WINDWARD WING BENDING MOMENT AT $\Phi = 45^\circ$: (a) ALPHA = 10° , (b) ALPHA = 25° , AND (c) ALPHA = 40°	51
22	LEEWARD WING LOADING AT $\Phi = 45^\circ$: (a) ALPHA = 10° , (b) ALPHA = 25° , AND (c) ALPHA = 40°	52
23	LEEWARD WING SHEAR AT $\Phi = 45^\circ$: (a) ALPHA = 10° , (b) ALPHA = 25° , AND (c) ALPHA = 40°	53
24	LEEWARD WING BENDING MOMENT AT $\Phi = 45^\circ$: (a) ALPHA = 10° , (b) ALPHA = 25° , AND (c) ALPHA = 40°	54
25	WINDWARD TAIL LOADING AT $\Phi = 45^\circ$: (a) ALPHA = 10° , (b) ALPHA = 25° , AND (c) ALPHA = 40°	55
26	WINDWARD TAIL SHEAR AT $\Phi = 45^\circ$: (a) ALPHA = 10° , (b) ALPHA = 25° , AND (c) ALPHA = 40°	56

ILLUSTRATIONS (Continued)

<u>Figure</u>		<u>Page</u>
27	WINDWARD TAIL BENDING MOMENT AT $\Phi = 45^\circ$: (a) ALPHA = 10° , (b) ALPHA = 25° , AND (c) ALPHA = 40°	57
28	LEEWARD TAIL LOADING AT $\Phi = 45^\circ$: (a) ALPHA = 10° , (b) ALPHA = 25° , AND (c) ALPHA = 40°	58
29	LEEWARD TAIL SHEAR AT $\Phi = 45^\circ$: (a) ALPHA = 10° , (b) ALPHA = 25° , AND (c) ALPHA = 40°	59
30	LEEWARD TAIL BENDING MOMENT AT $\Phi = 45^\circ$: (a) ALPHA = 10° , (b) ALPHA = 25° , AND (c) ALPHA = 40°	60
31	EFFECT OF WING DEFLECTION AT $\alpha = 10^\circ$, $\Phi = 0^\circ$: (a) BODY LOADING, (b) BODY SHEAR, AND (c) BODY BENDING MOMENT	61
32	EFFECT OF WING DEFLECTION AT $\alpha = 10^\circ$, $\Phi = 0^\circ$: (a) WING LOADING, (b) WING SHEAR, AND (c) WING BENDING MOMENT	62
33	EFFECT OF WING DEFLECTION AT $\alpha = 10^\circ$, $\Phi = 0^\circ$: (a) TAIL LOADING, (b) TAIL SHEAR, AND (c) TAIL BENDING MOMENT.....	63

1.0 INTRODUCTION

The Naval Surface Warfare Center, Dahlgren Division (NSWCDD) Aeroprediction Code (AP95)¹ allows the computation of aerodynamics over an extensive range of flight conditions which includes the operating environments encountered by most tactical missiles. This range covers angles of attack (AOA) up to 90 deg, Mach numbers from 0 to 15, and control deflections from -30 to +30 deg. Originally, it was limited to the roll position of $\Phi = 0$ deg (fins in the plus (+) position), but Reference 2 recently extended the code to the $\Phi = 45$ deg (fins in the cross (x) position) roll orientation.

The latest public release of the AP95 code incorporates the capability to model nonlinear aerodynamic loads. These nonlinear loads are estimated in an approximate analytical or semiempirical sense by separating each aerodynamic force component into a linear and nonlinear term. As in previous versions of the code, the linear term is modeled by the application of either linear, slender body, or second-order theory. The resulting pressure distributions can be integrated to produce aerodynamic loading information for use in structural design and analysis. The nonlinear contribution, however, is modeled by the direct application of wind tunnel data bases and is defined primarily in terms of total force and moment measurements. Some distribution information is provided for the nonlinear component of the body loads, but none is currently available for the lifting surface loads or for their interference effects on the body. This situation is not restrictive in terms of aerodynamic and performance analysis. Structural engineers, however, need to know not only the magnitude of the aerodynamic forces, but also how they are distributed over the surface of a missile if they are to determine the shear and bending moments to which its components will be subjected. For this reason, the AP95 code is being modified to allow the prediction of the distribution of the nonlinear, as well as the linear, aerodynamic loads over both the body and control surfaces. All interference effects will be included in the analysis in addition to the individual component nonlinear aerodynamics. It is believed that the next version of the Aeroprediction code (AP98) will be the first code of its kind to offer this capability.

2.0 ANALYSIS

The total normal force for a wing-body-tail configuration can be defined by:

$$C_N = C_{N_B} + C_{N_{W(B)}} + \Delta C_{N_{B(W)}} + C_{N_{T(B)}} + \Delta C_{N_{B(T)}} + C_{N_{T(V)}} \quad (1)$$

The first term in Equation (1) is the normal force coefficient of the body alone. The second term is the normal force coefficient of the wing in the presence of the body and the third represents the additional component of normal force on the body due to the presence of the wing. The fourth term is the normal force coefficient of the tail in the presence of the body and the fifth represents the incremental normal force on the body as a result of the tail. The final term is the normal force on the tail, usually negative, caused by the vortices shed from the wing.

Each of the terms in Equation (1) has a linear and a nonlinear component. Either linear theory or slender body theory is used to determine the linear portion of each term and the nonlinear contributions are computed directly from wind tunnel data bases with engineering judgment and extrapolation being used where data base information is limited. Overall average accuracy is maintained at ± 10 percent for the total normal and axial force coefficients and ± 4 percent of total body length for the center of pressure.

In the following sections, each component of Equation (1) will be considered individually and the methodology which has been developed to distribute its nonlinear elements over the body surface will be presented. First, the $\Phi = 0$ deg roll position will be addressed and then any changes or additions which are necessary to extend the methodology to the $\Phi = 45$ deg roll position will be presented.

2.1 BODY LOADS AT THE $\Phi = 0$ DEG ROLL POSITION

Four of the terms in Equation (1) contribute to the body loading. These are C_{N_b} , $\Delta C_{N_{b(w)}}$, $\Delta C_{N_{b(t)}}$, and $C_{N_{t(v)}}$. Only the first three of these will be discussed in this section. The wing-tail interference will be reserved for the section on lifting surface loads since it is connected directly to them and is shared with the tail surfaces.

2.1.1 Body Alone Loads

The body alone component, C_{N_b} , is composed of a linear and a nonlinear load. The linear load is computed analytically above $M = 1.2$ by either Van Dyke's hybrid theory³ or second order shock-expansion theory.⁴ Pressure coefficients are computed as a function of position along and around the body and then integrated along the body to obtain local linear normal force. That is

$$(c_{n_b})_L = \left(\frac{dC_{N_b}}{dx} \right)_L = \left(\frac{-2}{\pi r^2} \right) \int_0^\pi C_p(x, \Phi) (\cos \Phi) r d\Phi \quad (2)$$

The nonlinear body normal force coefficient contribution is

$$(C_{N_b})_{NL} = \eta C_{D_c} \frac{A_p}{A_{REF}} \sin^2 \alpha \quad (3)$$

If we assume that the nonlinear load is distributed uniformly along the body surface, then the local nonlinear normal force contribution at any point x is

$$(c_{n_b})_{NL} = \left(\frac{dC_{N_b}}{dx} \right)_{NL} = \frac{\eta C_{D_c} \sin^2 \alpha}{A_{REF}} r(x) . \quad (4)$$

The total local normal force coefficient at any point along the body surface is the sum of Equations (2) and (4).

$$c_{n_b} = (c_{n_b})_L + (c_{n_b})_{NL} \quad (5)$$

Comparison of Equation (5) with results from Computational Fluid Dynamics (CFD) computations indicated that the predicted body load in the nose region was too high at low AOA. It is believed that this discrepancy occurs because, at low AOA, the point at which the body vortices begin to separate is toward the afterbody of the missile. Then, as AOA is increased, the separation point moves forward and the full effect of the body shed vortices is apparent. In order to account for this effect, the nonlinear load contribution is adjusted as follows:

$$x \leq L_{NOSE}, \alpha < 30^\circ:$$

$$(c_{n_b})_{NL,ADJ} = \left(\frac{\alpha}{30} \right) (c_{n_b})_{NL} \quad (6)$$

$$L_{NOSE} < x < L_{NOSE} + 2D_B:$$

$$(c_{n_b})_{NL,ADJ} = \left[(c_{n_b})_{NL} \right]_{x=L_{NOSE}} + \left(\frac{x - L_{NOSE}}{2D_B} \right) \left((c_{n_b})_{NL} - \left[(c_{n_b})_{NL} \right]_{x=L_{NOSE}} \right) \quad (7)$$

$$x \geq L_{NOSE} + 2D_B:$$

$$(c_{n_b})_{NL,ADJ} = (c_{n_b})_{NL} + \left[(c_{n_b})_{NL} \right]_{NOSE} + \left[(c_{n_b})_{NL} \right]_{TRAN} \quad (8)$$

On the nose itself, as shown in Equation (6), the nonlinear load is reduced at AOA below $\alpha = 30$ deg by a factor which varies linearly with AOA from 1 at $\alpha = 30$ deg to 0 at $\alpha = 0$ deg. No adjustment is made at AOA above 30 deg. There is a transition region, which extends for a distance of two calibers from the end of the nose, within which the nonlinear load component is allowed to recover gradually from its reduced value at the end of the nose to its normally computed level at the current location, as shown in Equation (7). Since the total normal force computed by AP95 agrees well with experimental results, the portion of the nonlinear loads which are removed from the nose and transition regions must be added back into the loads on the

remainder of the body. Thus, Equation (8) shows that, for points on the body more than two calibers downstream of the nose, the normally computed local nonlinear loads are increased by two terms $\left[(c_{n_B})_{NL} \right]_{NOSE}$ and $\left[(c_{n_B})_{NL} \right]_{TRAN}$ which represent the total load reductions in the nose and transition regions, respectively, spread evenly over the total remaining body length. Figure 1 shows the effect of this change on the body loads for a typical case, using the SEASPARROW air-to-air missile as an example. As can be seen, relative to the CFD results which are shown for comparison, there is some improvement in the nose region and little change elsewhere.

2.1.2 Body-Wing and Body-Tail Interference Loads

For the discussion to follow, forward lifting surfaces will be referred to as wings and aft lifting surfaces will be referred to as the tail. In the vicinity of any lifting surface, the body is subjected to increased loads caused by interference effects. These contributions, represented in Equation (1) by $\Delta C_{N_{B(W)}}$ for the wing and by $\Delta C_{N_{B(T)}}$ for the tail, are also computed as separate linear and nonlinear components with afterbody effects being considered for the rear lifting surfaces. For simplicity, it was first assumed that these interference loads were distributed uniformly along the root chord of the wing or tail, thus affecting the body loading only along the attachment line from the leading edge to the trailing edge. These constant local loading values were defined as

$$\Delta c_{n_{B(W)}} = \frac{\Delta C_{N_{B(W)}}}{(C_r)_W} \quad (9)$$

and

$$\Delta c_{n_{B(T)}} = \frac{\Delta C_{N_{B(T)}}}{(C_r)_T} \quad (10)$$

Figure 2(a) shows the region of the body affected by these loads and Figure 2(b) shows the distribution of their magnitude. Comparisons with CFD data indicated that this approach produced interference effects which were too localized, with excessively high values along the root chords and none of the carryover load behind the lifting surfaces indicated by the data. Therefore, the region of influence of the lifting surfaces was changed to coincide with the area on the body surface bounded by the Mach lines coming from their leading and trailing edges, as shown in Figure 3(a). The new distribution of the load magnitude on the body is shown in Figure 3(b). It is consistent with the method currently used for moment and center of pressure calculations in the AP95. Note that the magnitude increases linearly from the leading edge to the point where the Mach lines from opposite lifting surfaces meet in the center of the body. Since the angle of the Mach lines, μ , is given by

$$\mu = \sin^{-1} \left(\frac{1}{M_L} \right) \quad (11)$$

the streamwise location where this intersection occurs is

$$x_2 = x_{LE} + \frac{\beta D_B}{2} \quad (12)$$

where

$$\beta = \sqrt{M_L^2 - 1} \quad (13)$$

The local Mach number, M_L , is approximated by the freestream Mach number. For the region on the body enclosed by both Mach lines, the entire body surface is affected by the interference and the load value is held constant at the maximum level. At the streamwise location given by

$$x_3 = x_{LE} + \frac{\beta D_B}{2} + C_r \quad (14)$$

the Mach lines from the trailing edges intersect and a portion of the body begins to emerge from the interference region until, at the point defined by

$$x_4 = x_{LE} + \beta D_B + C_r \quad (15)$$

all Mach lines have moved off the body and the interference loads are reduced to zero. Between x_3 and x_4 , the interference load is allowed to decay linearly from its maximum value to zero.

Since the total value of the interference normal force contribution must remain the same as for the uniform distribution originally assumed, it is necessary to adjust the maximum value of the local interference load relative to the constant value of Equations (9) and (10) and Figure 2(b). Since both the wing and the tail adjustments are handled in an identical manner, the W and T subscripts will be dropped and only one set of relations will be shown. The maximum values will become

$$\left[\Delta c_{n_B} \right]_{MAX} = \Delta c_{n_B} \left(\frac{2(C_r)}{2(C_r) + \beta D_B} \right) \quad (16)$$

Thus, a trapezoidal load pattern is produced, defined by

$$x_{LE} \leq x < x_2:$$

$$\Delta c_{n_B} = \left(\frac{x - x_{LE}}{x_2 - x_{LE}} \right) \left[\Delta c_{n_B} \right]_{MAX} \quad (17)$$

$$x_2 \leq x \leq x_3:$$

$$\Delta c_{n_B} = [\Delta c_{n_B}]_{MAX} \quad (18)$$

$$x_3 < x \leq x_4:$$

$$\Delta c_{n_B} = \left(1 - \frac{x - x_3}{x_4 - x_3}\right) [\Delta c_{n_B}]_{MAX} \quad (19)$$

In situations where the wing or tail is located near the aft end of the body, it is possible for the Mach lines to extend beyond the body and some of the interference loading will be lost unless further adjustments are made. For these cases, the cross-sectional area of the body enclosed by the Mach lines and the aft end of the body is determined and compared to the total cross-sectional area that would be enclosed by the Mach lines if the body were not cut off. The maximum interference load values are then adjusted to compensate for the lost area and maintain the correct total of interference normal force as computed by the AP95.

2.2 LIFTING SURFACE LOADS AT THE $\Phi = 0$ DEG ROLL POSITION

The total contributions to the normal force of the wing and tail are represented in Equation (1) by $C_{N_{W(B)}}$ and $C_{N_{T(B)}}$, respectively. Using $C_{N_{W(B)}}$ as an example, these two terms each have the following form:

$$C_{N_{W(B)}} = [K_{W(B)} \sin \alpha + k_{W(B)} \sin \delta] (C_{N_\alpha})_W \quad (20)$$

Nonlinearities are introduced into $C_{N_{W(B)}}$ by defining both a linear and a nonlinear contribution for the normal force of the isolated wing, represented by $(C_{N_\alpha})_W$, and for each of the interference factors $K_{W(B)}$ and $k_{W(B)}$ which are introduced to account for the effects of the presence of a body on the normal force of the lifting surface. The method which has been developed to distribute the nonlinear contributions to the wing-alone normal force and the interference factors will be presented in the next section.

The final term in Equation (1), $C_{N_{T(v)}}$, is also associated with the lifting surfaces. It represents the impact on the tail of vortices shed from the wing when both sets of lifting surfaces are present. A portion of this downwash effect should be allocated to the body, since it also experiences the effect of the shed vortices. Techniques to accomplish both the body/tail division of this load contribution as well as its spanwise distribution along the tail surfaces will be presented below.

2.2.1 Nonlinear Wing or Tail Alone and Interference Factor Load Distributions

The linear part of the local normal force coefficient on a wing or tail surface at a spanwise location y is

$$[c_n(y)]_L = \frac{1}{c(y)} \int_{x_{LE}}^{x_{TE}} \Delta C_p(x, y) dx \quad (21)$$

$\Delta C_p(x, y)$ is the difference between the pressure on the upper and lower surfaces at a given (x, y) location. This pressure differential is computed from either lifting surface theory for subsonic flows or 3-D thin wing theory for supersonic flows. Equation (21) gives the spanwise distribution of the linear contribution to the normal force of an isolated lifting surface. The total linear contribution to normal force can be found by integrating Equation (21) in the spanwise direction.

The nonlinear part of the wing alone lift is determined using a fourth order analytical method⁵ in conjunction with wing alone data bases.^{6,7,8} Only the total values of lift and moment are available from the data bases with no surface distribution information included. This distribution will be determined in conjunction with that of the interference factors.

From the combined linear and nonlinear wing-alone normal force, C_{N_α} is determined based on a secant slope of the total angle of attack, $|\alpha + \delta|$, experienced by the lifting surface. This slope is then multiplied by $\sin \alpha$ and $\sin \delta$ terms which contain the interference factors K and k , respectively, to account for the interference effects of the body on the wing. (All subscripts have been dropped from K and k for simplicity.) The linear contributions to K and k are found from slender body theory. These linear values are then adjusted for nonlinear^{6,7,9} effects based on information from wind tunnel data bases. As for the wing-alone case, these data bases provide only total force and moment measurements and, therefore, a method must be developed to distribute the nonlinear component of K and k along the span.

As shown above in Equation (21), the AP95 code already computes the spanwise distribution of the linear normal force of an isolated lifting surface. It will be assumed that the nonlinear contributions to the wing-alone normal force and to the interference effects, represented by the K and k factors, will be distributed in the same manner. Thus, at any y location, the local load $c_n(y)$ for the wing and tail will be

$$(c_n(y))_w = ([c_n(y)]_L)_w \left(\frac{C_{N_{w(B)}}}{\sum_{SPAN} ([c_n(y)]_L)_w} \right) \quad (22)$$

and

$$(c_n(y))_T = ([c_n(y)]_L)_T \left(\frac{C_{N_{T(B)}}}{\sum_{SPAN} ([c_n(y)]_L)_W} \right). \quad (23)$$

2.2.2 Wing-Tail Interference

The AP95 code computes only the total value of the wing-tail interference term ($C_{N_{T(v)}}$ in Equation (1)). In this instance, however, not only is a method of spanwise distribution on the tail needed, but it is also apparent that a portion of the downwash effects should be carried over to the body. The division of $C_{N_{T(v)}}$ between the tail and body will be considered first. The method in which this objective is accomplished is not rigorous, but does have some intuitive foundation and is probably as well as can be done with the limited amount of CFD data available.

Refer to Figure 4 for the geometry of this model. The assumption is made, from slender body theory, that the vortices from the forward lifting surfaces are shed from a spanwise location, y_{VORT} , of

$$y_{VORT} = \left(\frac{\pi}{4} \right) \left(\frac{b_W}{2} \right) + \frac{D_B}{2} \quad (24)$$

and travel straight back parallel to the velocity vector from this point. A relative value for the effect of this shed vortex on the tail surface at any spanwise point is given by

$$VC(y) = \left(\frac{1}{r_{VORT} + y_{DIST}} \right)^2 c(y)_T \quad (25)$$

where

$$y_{DIST} = |y_{VORT} - y| \quad (26)$$

and r_{VORT} is a "vortex radius" taken to be 0.04. This value of r_{VORT} could be subject to adjustment in the future as additional CFD or experimental data becomes available. An inspection of Equation (25) shows that, at any point y , it consists of the product of a factor which is proportional to the local vortex strength through the inverse square distance term and a second factor, represented by the local chord, which is related to the local area affected by the vortex. The use of an absolute value for y_{DIST} assures that the relation will be valid regardless of where the vortex location falls on the tail span, even if it lies outboard of the tip. The function of r_{VORT} is to prevent singularities if this distance becomes zero. On the body, a similar relation is used.

$$VC(y) = \left(\frac{1}{r_{VORT} + y_{DIST}} \right)^2 (C_r)_T \quad (27)$$

Note that the use of the root chord for the area factor assumes that only the body area directly between the tail surfaces is affected. This assumption is not strictly correct, but it offers a starting point until further refinements can be made.

Using these relations, the apportionment of the wing-tail interference losses can be accomplished by summing the VC terms for both the body and tail and then taking the ratios of the summations to their combined total.

$$[C_{N_{T(v)}}]_{BODY} = C_{N_{T(v)}} \left(\frac{\sum_{BODY} VC(y)}{\sum_{BODY} VC(y) + \sum_{TAIL} VC(y)} \right) \quad (28)$$

$$[C_{N_{T(v)}}]_{TAIL} = C_{N_{T(v)}} \left(\frac{\sum_{TAIL} VC(y)}{\sum_{BODY} VC(y) + \sum_{TAIL} VC(y)} \right) \quad (29)$$

It will be assumed that the portion of the wing-tail interference load which is allocated to the body by Equation (28) is distributed evenly along the body directly between the tail surfaces.

$$(c_{n_b})_{T(v)} = \frac{[C_{N_{T(v)}}]_{BODY}}{(C_r)_T} \quad (30)$$

This additional contribution is added to the total local body load at streamwise locations between the leading and trailing edges of the tail surfaces.

The portion of the wing-tail interference loads assigned to the tail surfaces by Equation (29) is distributed across the span of the tail by assuming that its magnitude at any y location is proportional to the VC(y) value (from Equation (25)) at that location.

$$(c_n(y))_{T(v)} = [C_{N_{T(v)}}]_{TAIL} \left(\frac{VC(y)}{\sum_{SPAN} VC(y)} \right) \quad (31)$$

These loads are added to those computed in Equation (23) to get the total local load at any spanwise location.

2.3 CHANGES FOR THE $\Phi = 45$ DEG ROLL POSITION

For the $\Phi = 45$ deg roll position, several changes must be made to the above methodology to produce a more accurate representation of the surface loads. It is obvious that there must be some way of accounting for the different aerodynamic environments experienced by the windward and leeward plane fins. In addition, the distribution of the body carryover loads induced by the lifting surfaces behave in a somewhat different fashion than for the $\Phi = 0$ deg case. The following sections describe the modifications that were made to the methodology described above to accommodate these differences.

2.3.1 Body-Wing and Body-Tail Interference Load Changes

The AP95 body alone normal force is considered to be independent of roll position. However, the body-wing and body-tail interference effects will change with the roll configuration. The $\Phi = 45$ deg interference factors are computed automatically when this option is selected in the input file and are simply substituted for $\Delta C_{N_{B(W)}}$ and $\Delta C_{N_{B(T)}}$ in all computations. The values of these interference factors were chosen to give good agreement with experiment for the total loads and center of pressure. Unfortunately, when compared to CFD data, it appears that they do not produce an accurate distribution of those loads along the body or on the leeward plane tail fins. There appear to be three physical phenomena which account for these discrepancies. The first of these will be discussed now and the others in the following section.

On the surface of the body between the lifting surfaces, there is a region of high dynamic pressure. Immediately behind the lifting surfaces, however, if there is an afterbody present, there is an area where the dynamic pressure is much lower. The current AP95 methodology at $\Phi = 45$ deg averages this difference out to get the right total normal force and adds a center of pressure shift which accounts for the inconsistencies in distribution. If the distribution of the body carryover loads is to be modeled correctly, some consideration must be given to the physics of the problem. What appears to be happening, based on the experimental data,¹ is that, in the region of the lifting surfaces, there is an enhancement to the body load at both the $\Phi = 0$ deg and $\Phi = 45$ deg roll positions. At $\Phi = 0$ deg, this enhancement can extend several body diameters downstream into the traditional Mach line influence region. The method employed to model this effect was discussed in Section 2.1.2. At $\Phi = 45$ deg, the body loads are influenced to a lesser extent in the immediate vicinity of the lifting surfaces, but are still much higher than in the body alone case. Downstream of the fins, however, the high dynamic pressure appears to decrease rapidly and produce a region of overexpansion where the body carryover actually becomes negative and total loads fall below those of the body alone. Thus, with an afterbody present, the body carryover load is lower than with no afterbody. (Note that the reverse is true at the $\Phi = 0$ deg roll orientation.)

Reference 2 models this effect with a lower minimum value of $K_{B(W)}$ at $\Phi = 45$ deg versus $\Phi = 0$ deg and a forward shift of the center of pressure. This approach does not, however, produce the proper distribution of the interference loads. For the present work, the following technique was used to accomplish this goal. It is first assumed that, for the purpose of computing the body carryover load distribution, the minimum value of $K_{B(W)}$ is the same at $\Phi = 45$ deg as it is at $\Phi = 0$ deg. This value of $[K_{B(W)}]_{MIN}$ is distributed in the vicinity of the lifting surfaces for both roll orientations as described in Section 2.1.2. However, for the $\Phi = 45$ deg roll position, an amount equal to

$$\Delta K_{B(W)} = \left([K_{B(W)}]_{MIN} \right)_{\Phi=0} - \left([K_{B(W)}]_{MIN} \right)_{\Phi=45} \quad (32)$$

is subtracted from $K_{B(W)}$ in the region downstream of position x_4 where x_4 is defined by Equation (15). Figure 5 shows how this negative load is distributed. It is assumed that

$$[\Delta C_{n_b}]_{MIN} = -[\Delta C_{n_b}]_{MAX} \quad (33)$$

and that the slope from x_4 to x_5 is the same as the slope from x_3 to x_4 . The slope from x_6 to x_7 is the negative of this value. The positive $\Delta C_{N_{B(W)}}$ contribution for $\Phi = 0$ deg has already been established and so the total negative contribution can be found as

$$\Delta C_{N_B}^- = [\Delta C_{N_B}]_{\Phi=0} - [\Delta C_{N_B}]_{\Phi=45} \quad (34)$$

where the W subscript has been dropped to avoid repetition. This relation and those to follow will be the same for both wing and tail surfaces. It can be seen that the total value of the body carryover term is not changed. The other defining parameters can be computed as follows:

$$x_5 = x_4 + (x_4 - x_3) \quad (35)$$

$$\Delta C_{N_B}^A = \frac{1}{2}(x_5 - x_4)[\Delta C_{N_B}]_{MIN} \quad (36)$$

$$\Delta C_{N_B}^C = \Delta C_{N_B}^A \quad (37)$$

$$\Delta C_{N_B}^B = \Delta C_{N_B}^- - (\Delta C_{N_B}^A + \Delta C_{N_B}^C) \quad (38)$$

$$x_6 = x_5 + \frac{\Delta C_{N_B}^B}{[\Delta C_{N_B}]_{MIN}} \quad (39)$$

$$x_7 = x_6 + (x_5 - x_4) \quad (40)$$

A trapezoidal distribution for the local negative contribution to the body loads can now be defined as follows:

$$x_4 \leq x < x_5:$$

$$\Delta c_{n_b} = \left(\frac{x - x_4}{x_5 - x_4} \right) \left[\Delta c_{n_b} \right]_{MIN} \quad (41)$$

$$x_5 \leq x \leq x_6:$$

$$\Delta c_{n_b} = \left[\Delta c_{n_b} \right]_{MIN} \quad (42)$$

$$x_6 < x \leq x_7:$$

$$\Delta c_{n_b} = \left(1 - \frac{x - x_6}{x_7 - x_6} \right) \left[\Delta c_{n_b} \right]_{MIN} \quad (43)$$

These local load components are added to the total local body loads within the specified streamwise locations. If there is insufficient afterbody length to allow the inclusion of the entire negative interference load, the remainder is carried over to the leeward tail surfaces.

2.3.2 Lifting Surface Load Changes

When a missile is rolled into the X ($\Phi = 45$ deg) position, the lower (windward plane) and upper (leeward plane) lifting surfaces will experience different aerodynamic environments. The normal force computed by the AP95 code is the total for all fins, both windward and leeward, and it must be divided between the two planes. In order to accomplish this division, the approach previously used in Reference 2 is employed. It is assumed, in agreement with slender body theory, that at an AOA of zero, the normal force is evenly distributed between the windward and leeward planes. As the AOA is increased, the load on the windward surfaces is increased linearly up to 90 percent of the total at $\alpha = 65$ deg. This percentage remains constant up to $\alpha = 90$ deg. On the other hand, the load on the leeward plane decreases in a corresponding fashion so that the total of the two is not changed. Thus, we have

$$\alpha \leq 65^\circ: \quad [c_n(y)]_{WINDWARD} = [c_n(y)] \left(0.5 + 0.4 \frac{\alpha}{65} \right) \quad (44)$$

$$[c_n(y)]_{LEEWARD} = [c_n(y)] \left(0.5 - 0.4 \frac{\alpha}{65} \right) \quad (45)$$

$$\alpha > 65^\circ: \quad [c_n(y)]_{WINDWARD} = 0.9[c_n(y)] \quad (46)$$

$$[c_n(y)]_{LEEWARD} = 0.1[c_n(y)] \quad (47)$$

A further point to consider is that the normal forces which are computed by the AP95 code are normal only to horizontal lifting surfaces in the $\Phi = 0$ deg roll orientation. In the $\Phi = 45$ deg case, the loads given by Equations (32)-(35) must be divided by $\cos \Phi$ on the windward side and by $\sin \Phi$ on the leeward side to give locally normal values.

The portion of the wing-tail interference, $C_{N_{T(v)}}$, which is allocated to the tail surfaces must also be divided between the windward and leeward planes. Once again relying on methodology developed in Reference 2, this division is accomplished using the wing-tail interference factors defined during the slender body derivation of this term. The mathematics of this process are quite involved and will not be repeated here. For more information, the reader may consult the cited reference. For the present purpose, if i_1 is the interference factor associated with the windward plane fin and i_4 the one with the leeward plane fin, then

$$[C_{N_{T(v)}}]_{WINDWARD} = [C_{N_{T(v)}}]_{TAIL} \left(\frac{i_1}{i_1 + i_4} \right) \quad (48)$$

and

$$[C_{N_{T(v)}}]_{LEEWARD} = [C_{N_{T(v)}}]_{TAIL} \left(\frac{i_4}{i_1 + i_4} \right) \quad (49)$$

This brings us to the second physical phenomenon which is not explicitly modeled in the approach outlined above. In the $\Phi = 45$ deg roll position, there is a "shadowing" effect on the leeward plane lifting surfaces for high Mach number flows. A "shadowed region" exists near the root chord where Newtonian theory predicts a pressure coefficient of zero. As a result, the predicted values of loads on the leeward plane lifting surfaces to be presented later will be high, but due to the complexities involved in trying to model this effect, no attempt has been made to do so at this time. The higher the Mach number, the more accurate the Newtonian prediction of zero pressure coefficient in the shadowed region becomes. This therefore means that the current leeward plane loads near the body will become less accurate as Mach number increases.

The final phenomenon which is believed to affect the load distributions but is not yet fully modeled involves the stronger influence of body vortices on the leeward plane fins as their location is moved farther aft on the body. In the development of the semi-empirical approach of the AP95, the body vortex effects were inherently included in the body carryover load. Hence, the body carryover load was lower for the tail fins than it should have been to offset the fact that the vortices actually cause the leeward plane tail fins to lose more normal force the farther aft they are located. To account for this fact, negative contributions from the adjusted body-lifting surface interference loads, as described in Section 2.3.1, which cannot be distributed on the afterbody due

to lack of sufficient length will be carried over to the leeward plane tail fins. They will be distributed along the span in the same manner as the linear and nonlinear lifting surface loads.

2.4 LOADS, SHEAR, AND BENDING MOMENTS

The primary purpose of computing load distributions over the components of a missile body is to allow the determination of shear and bending moment within the structural members. The loads which have been determined so far are non-dimensional in the sense that they represent a normal force coefficient per unit length. Multiplying them by the dynamic pressure and the reference area will give local loads in pounds per foot. These loads can be integrated to get the local shear in pounds and the shear can in turn be integrated to get the local moment in pound-feet. For the body, utilizing the results of Equations (2), (6), (7), (8), (17), (18), (19), and (30), we have for the dimensionalized local loads $w(x)$

$$w(x)_B = \left[(c_{n_B})_L + (c_{n_B})_{NL,ADJ} + \Delta c_{n_B(w)} + \Delta c_{n_B(T)} + (c_{n_B})_{T(V)} \right] Q A_{REF} \quad (50)$$

where

$$Q = \frac{\gamma}{2} P_\infty M_\infty^2 \quad (51)$$

and

$$A_{REF} = \pi \frac{D_B^2}{4} \quad (52)$$

We can then integrate to get the shear, $V(x)_B$, and the bending moment, $BM(x)_B$.

$$V(x)_B = \int_0^x w(x)_B dx \quad (53)$$

$$BM(x)_B = \int_0^x V(x)_B dx \quad (54)$$

The procedure for the lifting surfaces is the same except for the spanwise rather than the streamwise variation of the loads. For the wing, using the nondimensional load from Equation (22), we get

$$w(y)_W = \left[(c_n(y))_W \right] Q A_{REF} \quad (55)$$

For the tail, there may be a contribution from the wing-tail interference given by Equation (30) in addition to the nondimensional load from Equation (23).

$$w(y)_T = \left[(c_n(y))_T + (c_n(y))_{T(V)} \right] Q A_{REF} \quad (56)$$

Equations (55) and (56), as presented above, are valid for the $\Phi = 0$ deg roll position. For the $\Phi = 45$ deg case, there will be separate loads for the windward and leeward sets of lifting surfaces. These separate loads can be computed simply by substituting the windward and leeward values of the $(c_n(y))_w$, $(c_n(y))_T$, and $(c_n(y))_{T(V)}$ contributions given in Equations (32)-(35). The integration for shear and bending moment will be the same for both lifting surfaces and for both roll orientations. With the W/T subscript indicating the appropriate value for either the wing or tail, we have

$$V(y)_{W/T} = \int_0^y w(y)_{W/T} dy \quad (57)$$

$$BM(y)_{W/T} = \int_0^y V(y)_{W/T} dy \quad (58)$$

All of the above integrations are performed in the AP95 code using the trapezoidal rule.

3.0 RESULTS AND DISCUSSION

For purposes of validation, the results computed by the new Aeroprediction methodology are compared to Navier-Stokes¹⁰ computer calculations performed by Clint Housh at the Naval Air Warfare Center Weapons Division (NAWCWPNS). Distributions of aerodynamic loads, shear, and bending moment were generated by both methods for the SEASPARROW air-to-air missile at Mach numbers of 1.50, 2.87, and 4.60 and angles of attack of 10, 25, and 40 deg. The SEASPARROW, shown in Figure 6, with its two sets of lifting surfaces, provides an opportunity to exercise all of the new additions to the code. The results of these computations are presented and discussed below. The general format followed is to handle each component (body, wing, tail) separately. First, the local loads are plotted on three separate graphs corresponding to the three angles of attack. All three Mach numbers are shown on the same plot. The shear and bending moment are then presented, in turn, in groups of three graphs corresponding to the angles of attack. This sequence is then repeated for the next missile component. In all cases, the CFD results are plotted together with the Aeroprediction results for comparison purposes. Before discussing the comparison of the semiempirical and CFD results, a brief discussion of the CFD methodology is in order.

3.1 CFD METHODOLOGY

For the purposes of validation, the results computed by the new Aeroprediction methodology are compared to Navier-Stokes¹⁰ computer calculations performed by Clint Housh at the Naval Air Warfare Center Weapons Division (NAWCWPNS). The configuration chosen to provide the validation data for the new semiempirical model was the SEASPARROW missile

configuration. This configuration was chosen because of the availability of experimental force and moment data,¹¹ which was used to provide a level of confidence in the CFD results. The configuration consisted of an ogive-cylinder body with a fineness ratio of 18, cruciform wings, and in-line tails. The wings had a trapezoidal planform with a leading-edge sweep of 45 deg and a diamond airfoil section. The tails had a delta planform with a leading-edge sweep of 57 deg and a modified diamond airfoil section. Additional geometrical detail can be found in Reference 11.

Computational grids were developed for the SEASPARROW geometry in both the "+" (roll angle $\Phi = 0$ deg) configuration, and the "x" (roll angle $\Phi = 45$ deg) configuration. The CFD grid-models for these analyses were developed using the Chimera overset mesh approach.¹² The Chimera overset mesh technique is a domain decomposition procedure where a configuration is meshed using a collection of overset grids. Grids for the individual components of a configuration are developed independently of one another and are overset upon the others. Because each component grid is generated independently (i.e., body grid, wing grid, tail grid), portions of one grid may lie inside the physical surfaces of another. These points are identified and excluded from the computations using the Pegasus computer program.¹³ The Pegasus code defines regions where holes are cut by one grid into another and provides the interpolation stencils, used by the flow solver, at the various grid interfaces. The grids of the individual components were developed using the Gridgen¹⁴ computer program.

Viscous grid spacing was employed over all of the solid surfaces in order to obtain accurate solutions to the Navier-Stokes equations. The grid spacing normal to solid walls was set to approximately 0.00004 body diameters, corresponding to y^+ values on the order of one. The grid model for the "+" configuration was made up of 7 separate grids totaling 2,131,950 grid points. The grid model for the "x" configuration has 5 grids consisting of 2,223,500 grid points.

The OVERFLOW¹⁰ computer program was used to provide solutions to the thin-layer formulation of the Reynolds-averaged Navier-Stokes equations. Among the many options available in the code, the ARC3D-based¹⁵ implicit 3-factor diagonal scheme was chosen to advance the solution in time. Conventional central differences were used to evaluate the inviscid and viscous terms in each computational direction. Second and fourth order smoothing were applied to both the right and left hand sides. Also, for the energy equation, the quantity ph was smoothed rather than pe . The Baldwin-Barth one-equation turbulence model¹⁶ was used for closure.

The boundary condition used for solid surfaces was that of an isothermal no-slip wall with pressure extrapolation. The downstream overflow boundary was set using simple extrapolation. The collapsed face from the tip of the nose to the upstream boundary plane was handled by setting the boundary value to an average of all surrounding cells by varying the circumferential index and holding the axial and normal indices constant. On the symmetry plane, the velocity normal to the plane was set to zero. The upstream boundary and far-field boundary values were set using a characteristic condition based on Riemann invariants. The entire flow field was initialized to free stream values appropriate to the experimental flow conditions described in Reference 11.

The solutions were run on a Silicon Graphics Incorporated (SGI) Power Challenge Array using a single R8000 processor. The OVERFLOW program was run with the namelist option: INCORE=FALSE. In this mode, memory requirements are set by the largest individual grid. Grid, flowfield and interpolation arrays are read from scratch files, one (or more) iterations are taken, and the flowfield is written back out to disk. The memory required to run these cases on the SGI machine was on the order of 9.4 Mwords (8-byte words). The processing time used by the computer, CPU time, was approximately 62.33 μ sec/grid point/iteration. A typical solution took 3000 iterations to converge the viscous and inviscid forces. Local time stepping was used to accelerate the solutions to steady state.

Solutions have been obtained for the SEASPARROW missile configuration at three supersonic Mach numbers ($M = 1.5, 2.87$ and 4.63), two roll angles ($\Phi = 0$ and 45 deg), and three different angles of attack ($\alpha = 10, 25$, and 40 deg). Table 1 shows a summary of the solutions obtained and the percent difference between experimental and Navier-Stokes computed lift and drag coefficients. Also shown is the difference in center of pressure location between experimental and computed results expressed as a percentage of the overall length of the missile. The comparisons between the experimental data and the computed results allow us to evaluate the accuracy of the solution and, to some extent, validate the solution methodology.

TABLE 1. SPARROW III RUN MATRIX

Mach Number	AOA α	Roll Φ	CL % diff exp vs. CFD	CD % diff exp vs. CFD	Xcp diff % body length exp vs. CFD
1.50	10	0	1.8	6.1	0.78
1.50	25	0	1.1	2.6	0.57
1.50	40	0	-0.7	0.4	0.07
2.87	10	0	2.1	5.9	1.44
2.87	25	0	-1.5	-0.7	0.07
2.87	40	0	-1.4	-2.9	0.38
4.60	10	0	0	-8.3	1.13
4.60	25	0	1.2	4.3	0.35
4.60	40	0	-6.1	-7.4	2.42
1.50	10	45	2.4	15.0	0.85
1.50	25	45	0.4	0.6	0.44
1.50	40	45	-1.5	-0.7	-0.09
2.87	10	45	-1.6	12.1	1.22
2.87	25	45	-3.0	3.1	0.77
2.87	40	45	-0.9	-0.8	0.56
4.60	10	45	-5.6	6.7	1.58
4.60	25	45	-0.6	3.6	1.21
4.60	40	45	0.5	1.8	0.82

As shown in the table, the average percent difference between experimental and CFD values of lift coefficient, for all of the solutions obtained, was slightly less than 2 percent. This is good agreement between the experimental and CFD results. A couple of the solutions did not predict the lift coefficient as well: the $M = 4.6$, $\alpha = 40$ deg, $\Phi = 0$ deg and the $M = 4.6$,

$\alpha = 10$ deg, $\Phi = 45$ deg cases. In these cases, the percent difference of lift coefficient was on the order of 6 percent. For these two cases the poor prediction of the magnitude of lift was also apparent in the center of pressure prediction.

Also shown in the table, the computed center of pressure was slightly aft of the experimental center of pressure for all of the cases run (except the $M = 1.5$, $\alpha = 40$ deg, $\Phi = 0$ deg case). The average difference between the experimental and computed center of pressure results was on the order of 1 percent of the body length for the solutions run. In addition, at each Mach number, the percent difference of drag coefficient between experimental and computed results was greater at the low angles of attack. This is not surprising considering the large increase in drag coefficient with angle of attack. If, for example, the experimental and computed drag coefficients are separated by a constant δ regardless of angle of attack, that δ is a larger percentage of a smaller number.

All in all, the CFD results compared favorably with the experimental data. The good agreement over the wide angle of attack range shows the solution methodology to be accurate in predicting both linear and nonlinear aerodynamics. The close agreement in the center of pressure prediction show the capability of the solution methodology to accurately model the load distribution. The good agreement validates the solution methodology and confirms the accuracy of the solutions obtained.

3.2 RESULTS FOR $\Phi = 0$ DEG ROLL POSITION

Comparisons of the body results from the new Aeroprediction methodology and the CFD computations are shown in Figures 7 through 9. Figure 7 shows the body loads. Agreement is, in general, quite good. However, even after the adjustments made to the nose, there is still some slight overprediction of the loads in this region. In addition, for the $M = 4.60$, $\alpha = 40$ deg case, there is some "smearing out" of the Aeroprediction body interference loads in the vicinity of the wing. This could be the result of shock interaction effects which are not modeled in the code. Figure 8 shows the comparisons for shear force at the same corresponding angles of attack. The Aeroprediction code does a very good job with some overprediction for the $\alpha = 10$ deg cases relative to the CFD results. Note that the shear results are very good for the $M = 4.60$, $\alpha = 40$ deg case cited above. The under and over prediction regions for local loads tend to cancel each other out when they are integrated to get the shear. The bending moment results for the body are plotted in Figure 9. Once again, agreement is quite good, with some slight overprediction at low α .

Figures 10-12 present the results for the wing. The local loads are shown in Figure 10. Agreement with the CFD results is excellent in most cases with the only exceptions being at $M = 4.60$ near the body where the loads are overpredicted. It is possible that there are some shock interaction effects which are not accounted for in this region. Wing shear results are plotted in Figure 11 and they are in very good agreement with the CFD results with only small overpredictions at $\alpha = 10$ deg. Bending moments, shown in Figure 12, are also predicted quite well with some slight underprediction at high α .

The tail comparisons are shown in Figures 13-15. The loads, presented in Figure 13, while not in quite as close agreement as for the wing, are still good, with the region near the wing root at high Mach number once again being overpredicted. Figure 14 shows the corresponding shear loads. The correlation with the CFD results is once again quite good with a small degree of overprediction, especially at $\alpha = 40$ deg. The bending moment results, shown in Figure 15, are in very good agreement.

3.3 RESULTS FOR $\Phi = 45$ DEG ROLL POSITION

Figure 16 shows the comparisons for the body loads. At $M = 1.50$, the Aeroprediction results exhibit good agreement with the CFD computations. However, at $M = 2.87$ and to an even greater extent at $M = 4.60$, the CFD predictions show a sharp rise for the body loads in the vicinity of the wings followed by a rapid decrease below body alone values behind the wings. This behavior is only partially captured in the Aeroprediction results which show a smoother rise with a lower peak and a lesser decline behind the wings. As discussed in Section 2.1.3, modifications were made to the body carryover methodology for the $\Phi = 45$ deg roll position to improve the modeling of this phenomenon. These changes have resulted in a great improvement in the code's performance in this region, but the sharp surface pressure variations are still not completely modeled. The physical mechanism which gives rise to the pressure spike and the following overexpansion is not completely understood at the present time and, since it is most likely associated with strong shock interactions on the surface, it is considered beyond the scope of the present work to try and develop a more rigorous model. Figure 17 shows the results for the shear force distributions. The agreement with the CFD results is quite good, especially considering the body load variations. The body bending moments, shown in Figure 18, exhibit even better agreement.

The spanwise load distributions for the windward plane wings are plotted in Figure 19. The agreement between the Aeroprediction and CFD results is very good with only some minor deviations for $M = 4.60$. The shear loads are shown in Figure 20. Again, the agreement is quite close with the Aeroprediction results being slightly high for $M = 4.60$ at the two lower angles of attack. The bending moments, presented in Figure 21, show a general tendency to be slightly low relative to the CFD results but overall agreement is good.

The load distributions for the leeward wings are shown in Figure 22. It can be seen that the "shadowing" effect discussed above is quite evident for the $M = 2.87$ and $M = 4.60$ cases. The CFD results predict a large pressure loss on the wings in the shadowed region near the body which is not modeled in the Aeroprediction code. Otherwise, agreement is very good. The shear distributions are shown in Figure 23, and, as might be expected, there is significant overprediction at the higher Mach numbers relative to the CFD results, but the results are still surprisingly good. The same comments apply to the bending moments which are presented in Figure 24.

Figure 25 shows the windward tail loads. The agreement between the two approaches is quite good except for the $M = 4.60$ case at $\alpha = 25$ deg. The CFD results show a loss of pressure on the inboard section of the tail surfaces which may be associated with a shock or vortex

impingement which is not modeled by the Aeroprediction code. With this exception, the shear and bending moment distributions, shown in Figures 26 and 27, respectively, show very good agreement.

The leeward tail loads are plotted in Figure 28. As for the leeward wings, the "shadowing" effect is very obvious at the two higher Mach numbers. The shear loads, shown in Figure 29, and the bending moments, shown in Figure 30, tend to overpredict relative to the CFD results because of this effect. It should be noted that by modifying the body carryover prediction methodology for the $\Phi = 45$ deg case and applying any excess negative contributions to the leeward tail, the results for the leeward tail have been improved substantially over their original values. However, because of the complex nature of leeside flow fields at high angles of attack, it is extremely difficult to develop empirical models that will give truly accurate results in these regions.

3.4 RESULTS FOR WING DEFLECTION

As a final check on the new additions to the code, a case was run at $M = 2.87$ and $\alpha = 10$ deg for a wing deflection of 20 deg. Only the $\Phi = 0$ deg roll position was considered. The resulting loads, shear, and bending moment for the body are shown in Figure 31. These loads reflect contributions from body-wing interference factors, $K_{B(W)}$ and $k_{B(W)}$, associated, respectively, with the total missile angle of attack and with the wing deflection angle. As should be expected, the curves for the undeflected and deflected case are identical up to the location of the wing where the body carryover load from the deflected wing is much higher than for the undeflected case. There is also a slightly lower load in the region of the tail when the wing is deflected because of the more negative wing-tail interference effect.

The curves for the loads, shear, and bending moment of the wing are presented in Figure 32. The results are once again as would be expected with higher values for all parameters when the wing is deflected.

Finally, Figure 33 show the loads, shear, and bending moment, respectively, for the tail. Note that, in this case, because of the more negative effect of the wing-tail interference, the loads on the tail are lower when the wing is deflected. The lower loads translate into lower values for the shear and bending moment as well.

4.0 SUMMARY

New methodology has been added to the NSWCDD Aeroprediction code to compute both the linear and nonlinear contributions to surface loads and to distribute these loads over the body and lifting surfaces. The new methods include models to simulate lifting surface interference effects on the body for both the $\Phi = 0$ deg and $\Phi = 45$ deg roll positions. At $\Phi = 45$ deg, load

distributions are computed for both the windward and leeward lifting surfaces. Wing-tail interference loads are now separated into separate components which are distributed along the body in the vicinity of the tail as well as across the tail surfaces themselves. All loads are integrated to give shear and bending moment distributions which may be used by structural engineers in the design process.

As an aid in developing the new techniques and for validation purposes, results from Navier-Stokes CFD computations for the SEASPARROW air-to-air missile were utilized. In general, the Aeroprediction methodology proved to be quite successful at modeling the distribution of surface loads when compared to the CFD results. The only exceptions occurred for the $\Phi = 45$ deg roll position where the loads on leeward lifting surfaces (especially tail surfaces) tended to be overpredicted, and the exaggerated pressure variations on the body in the vicinity of lifting surfaces were not fully captured.

With these new additions, the Aeroprediction code should prove to be a much more useful tool to the structural engineer who is interested in performing preliminary structural analyses of several competing missile designs.

5.0 REFERENCES

1. Moore, F. G.; McInville, R. M.; and Hymer, T. C., *The 1995 Version of the NSWC Aeroprediction Code: Part I - Summary of New Theoretical Methodology*, NSWCDD/TR-94/379, Feb 1995.
2. Moore, F. G. and McInville, R. M., *Extension of the NSWCDD Aeroprediction Code to the Roll Position of 45 Degrees*, NSWCDD/TR-95/160, Dec 1995.
3. Van Dyke, M. D., *First and Second Order Theory of Supersonic Flow Past Bodies of Revolution*, JAS, Vol 18, No 3, Mar 1951, pp 161-175.
4. Moore, F. G.; Armistead, M. A.; Rowles, S. H.; and DeJarnette, F. R., *Second-Order Shock-Expansion Theory Extended to Include Real Gas Effects*, NAVSWC TR 90-683, Feb 1992.
5. Moore, F. G. and McInville, R. M., *A New Method for Calculating Wing Alone Aerodynamics to Angle of Attack 180°*, NSWCDD/TR-94/3, Mar 1994.
6. Stallings, R. L. and Lamb, M., *Wing Alone Aerodynamic Characteristics for High Angles of Attack at Supersonic Speeds*, NASA Technical Paper 1889, Jul 1981.
7. Baker, W. B., Jr., *Static Aerodynamic Characteristics of Generalized Slender Bodies With and Without Fins at Mach Numbers from 0.6 to 3.0 and Angles of Attack from 0 to 180°*, AEDC-TR-75-124, Vol I and II, May 1976, Tullahoma, TN.
8. Nielsen, J. N.; Hensch, M. J.; and Smith, C. A., *A Preliminary Method for Calculating the Aerodynamic Characteristics of Cruciform Missiles to High Angles of Attack Including Effects of Roll Angle and Control Deflections*, ONR-CR215-226-4F, 800 N. Quincy St., Arlington, VA 22217.
9. NASA Langley Research Center Tri-Service Missile Data Base, Transmitted from NASA/LRC Jerry M. Allen to NSWCDD on 5 Nov 1991 (formal documentation in progress).
10. Buning, P. G., et al., *Overflow User's Manual*, Version 1.6an, Jun 1995.

REFERENCES (Continued)

11. Monta, W. J., *Supersonic Aerodynamic Characteristics of a Sparrow III Type Missile Model With Wing Controls and Comparison With Existing Tail-Control Results*, NASA Technical Paper 1078, Oct 1977.
12. Benek, J. A.; Buning, P. G.; and Steger, J. L., *A 3-D Chimera Grid Embedding Technique*, AIAA Paper 85-1523, Jul 1985.
13. Suhs, N. E. and Tramel, R. W., *PEGASUS 4.0 User's Manual*, AEDC-TR-91-8, Arnold Engineering Development Center, Nov 1991.
14. GRIDGEN, *User's Manual For Gridgen Version 11*, Pointwise, Inc., Feb 1996.
15. Pulliam, T. H., *Euler and Thin Layer Navier Stokes Codes: ARC2D and ARC3D*, Notes for Computational Fluids Dynamics Workshop, University of Tennessee Space Institute, Mar 1984.
16. Baldwin, B. S. and Barth, T. J., *A One-Equation Turbulence Transport Model for High Reynolds Number Wall-Bounded Flows*, NASA TM 102847, Aug 1990.

6.0 SYMBOLS AND DEFINITIONS

AOA	Angle of Attack
AP95	Aeroprediction 1995
AP98	Aeroprediction 1998
CFD	Computational Fluid Dynamics
NAWCWPNS	Naval Air Warfare Center, Weapons Division
NSWCDD	Naval Surface Warfare Center, Dahlgren Division
A_p	Planform area of the body in the crossflow plane (ft ²)
A_{REF}	Reference area (maximum cross-sectional area of body, if a body is present, or planform area of wing if wing alone) (ft ²)
b_T	Tail span (not including body) (ft)
b_w	Wing span (not including body) (ft)
$BM(x)_B$	Body bending moment as a function of streamwise coordinate (lb-ft)
$BM(y)_{w/T}$	Wing or tail bending moment as a function of spanwise coordinate (lb-ft)
$c(y)$	Local chord of lifting surface as a function of spanwise coordinate (ft)
$c(y)_T$	Local chord of tail as a function of spanwise coordinate (ft)
$c(y)_w$	Local chord of wing as a function of spanwise coordinate (ft)
c_{n_B}	Local normal force coefficient of the body
$(c_{n_B})_L$	Linear component of body local normal force coefficient
$(\Delta c_{n_B})_{MAX}$	Maximum value of local body normal force coefficient in trapezoidal distribution of positive lifting surface interference contribution
$(\Delta c_{n_B})_{MIN}$	Minimum value of local body normal force coefficient in trapezoidal distribution of negative lifting surface interference contribution

$(c_{n_B})_{NL}$	Nonlinear component of body local normal force coefficient
$(c_{n_B})_{NL,ADJ}$	Nonlinear component of body local normal force coefficient adjusted for decreased nose loads
$[(c_{n_B})_{NL}]_{NOSE}$	Component of body local nonlinear normal force coefficient, downstream of nose, added to make up for decrease of normal force on nose
$[(c_{n_B})_{NL}]_{TRAN}$	Component of body local nonlinear normal force coefficient, downstream of nose, added to make up for loss of normal force in transition region
$[(c_{n_B})_{NL}]_{x=L_{NOSE}}$	Nonlinear component of body local normal force coefficient at end of nose
$(c_{n_B})_{T(V)}$	Component of body local normal force coefficient due to wing-tail interference
$[c_n(y)]_L$	Linear component of local normal force coefficient on lifting surfaces as a function of spanwise coordinate
$[(c_n(y))_L]_T$	Linear component of local normal force coefficient on tail as a function of spanwise coordinate
$[(c_n(y))_L]_W$	Linear component of local normal force coefficient on wing as a function of spanwise coordinate
$[c_n(y)]_{LEEWARD}$	Portion of total local normal force coefficient assigned to the leeward lifting surfaces
$(c_n(y))_T$	Local normal force coefficient on tail as a function of spanwise coordinate
$(c_n(y))_{T(V)}$	Portion of local normal force coefficient on lifting surfaces attributed to wing-tail interference

$(c_n(y))_w$	Local normal force coefficient on wing as a function of spanwise coordinate
$[c_n(y)]_{WINDWARD}$	Portion of total local normal force coefficient assigned to the windward lifting surfaces
C_N	Total normal force coefficient
C_{N_B}	Normal force coefficient of the body
$\Delta C_{N_B}^-$	Total negative contribution of lifting surface interference to body normal force
$\Delta C_{N_B}^A$	Body normal force coefficient contribution from region A of trapezoidal distribution
$\Delta C_{N_B}^B$	Body normal force coefficient contribution from region B of trapezoidal distribution
$\Delta C_{N_B}^C$	Body normal force coefficient contribution from region C of trapezoidal distribution
$\left(\frac{dC_{N_B}}{dx}\right)_L$	Linear component of streamwise variation of body normal force coefficient (ft ⁻¹)
$\left(\frac{dC_{N_B}}{dx}\right)_{NL}$	Nonlinear component of streamwise variation of body normal force coefficient (ft ⁻¹)
$(C_{N_B})_L$	Linear component of the body normal force coefficient
$(C_{N_B})_{NL}$	Nonlinear component of the body normal force coefficient
$\Delta C_{N_B(T)}$	Increment to normal force coefficient on body due to presence of tail
$\Delta C_{N_B(W)}$	Increment to normal force coefficient on body due to presence of wing

$\left[\Delta C_{N_B} \right]_{\Phi=45^\circ}$	Contribution to body normal force due to presence of a lifting surface at $\Phi = 45$ deg roll position
$C_{N_{T(B)}}$	Normal force coefficient of tail in presence of body
$C_{N_{T(V)}}$	Component of normal force coefficient in tail region due to interference from wing
$\left[C_{N_{T(V)}} \right]_{BODY}$	Portion of total wing-tail interference term assigned to body
$\left[C_{N_{T(V)}} \right]_{LEEWARD}$	Portion of tail component of wing-tail interference term assigned to the leeward tail surfaces
$\left[C_{N_{T(V)}} \right]_{TAIL}$	Portion of total wing-tail interference term assigned to tail
$\left[C_{N_{T(V)}} \right]_{WINDWARD}$	Portion of tail component of wing-tail interference term assigned to the windward tail surfaces
$C_{N_{W(B)}}$	Normal force coefficient of the wing in the presence of the body
$(C_{N_\alpha})_W$	Change of wing normal force coefficient with angle of attack (rad^{-1})
C_P	Pressure coefficient
C_r	Root chord of lifting surface (ft)
$(C_r)_T$	Root chord of tail (ft)
$(C_r)_W$	Root chord of wing (ft)
C_{D_c}	Crossflow drag coefficient
D_B	Diameter of body (ft)
e	internal energy (ft^2/sec^2)
i_1, i_4	Interference factors in wing-tail interference calculations for windward and leeward plane wings, respectively

h	local enthalpy (ft ² /sec ²)
k	Ratio of normal force contribution of a deflected lifting surface in the presence of a body to that of the lifting surface alone at $\alpha = 0$ deg
$k_{B(W)}$	Ratio of additional body normal force coefficient due to the presence of a deflected wing to that of the wing alone at $\alpha = 0$ deg
$k_{W(B)}$	Ratio of normal force contribution of a deflected wing in the presence of a body to that of the wing alone at $\alpha = 0$ deg
K	Ratio of lifting surface normal force coefficient in the presence of a body to that of the lifting surface alone at $\delta = 0$ deg
$K_{B(W)}$	Ratio of additional body normal force coefficient in the presence of a wing to that of the wing alone at $\delta = 0$ deg
$\Delta K_{B(W)}$	Difference between minimum $K_{B(W)}$ value at $\Phi = 0$ deg and $\Phi = 45$ deg
$[K_{B(W)}]_{MIN}$	Minimum value of $K_{B(W)}$
$([K_{B(W)}]_{MIN})_{\Phi=0^\circ}$	Minimum value of $K_{B(W)}$ at the $\Phi = 0$ deg roll position
$([K_{B(W)}]_{MIN})_{\Phi=45^\circ}$	Minimum value of $K_{B(W)}$ at the $\Phi = 45$ deg roll position
$K_{W(B)}$	Ratio of wing normal force coefficient in the presence of a body to that of the wing alone at $\delta = 0$ deg
L_{NOSE}	Length of the nose
M	Mach number
M_L	Local Mach number
M_∞	Freestream Mach number
P_∞	Freestream pressure (lb/ft ²)
Q	Dynamic pressure (lb/ft ²)
r	Local body radius (ft)
Γ_{VORT}	Vortex radius (ft)

$VC(y)$	Vortex strength-local chord parameter
$V(x)_B$	Body shear as a function of streamwise coordinate (lb)
$V(y)_{WT}$	Wing or tail shear as a function of spanwise coordinate (lb)
$w(x)_B$	Local body load as a function of streamwise coordinate (lb/ft)
$w(y)_T$	Local tail load as a function of spanwise coordinate (lb/ft)
$w(y)_W$	Local wing load as a function of spanwise coordinate (lb/ft)
x	Streamwise coordinate (ft)
x_{LE}	Streamwise location of leading edge (ft)
x_{TE}	Streamwise location of trailing edge (ft)
x_2, x_3, x_4	Streamwise coordinates used to define the trapezoidal distribution of the positive body-lifting surface interference region (ft)
x_5, x_6, x_7	Streamwise coordinates used to define the trapezoidal distribution of the negative body-lifting surface interference region (ft)
y	Spanwise lifting surface coordinate (ft)
y_{DIST}	Spanwise distance from path of vortex shed from wing to local point on tail (ft)
y_{VORT}	Spanwise distance from centerline of body to path of vortex shed from wing
α	Angle of attack (rad, deg)
β	$\sqrt{M^2 - 1}$
γ	Specific heat ratio of air
δ	Deflection angle of control surface (rad, deg)
η	Parameter used in viscous crossflow theory for nonlinear body normal force (in this context, it is the ratio of the normal force of a circular cylinder of given length-to-diameter ratio to that of a cylinder of infinite length)

ρ	density (slugs/ft ³)
Φ	Roll position of missile ($\Phi = 0$ deg corresponds to fins in the plus (+) orientation)

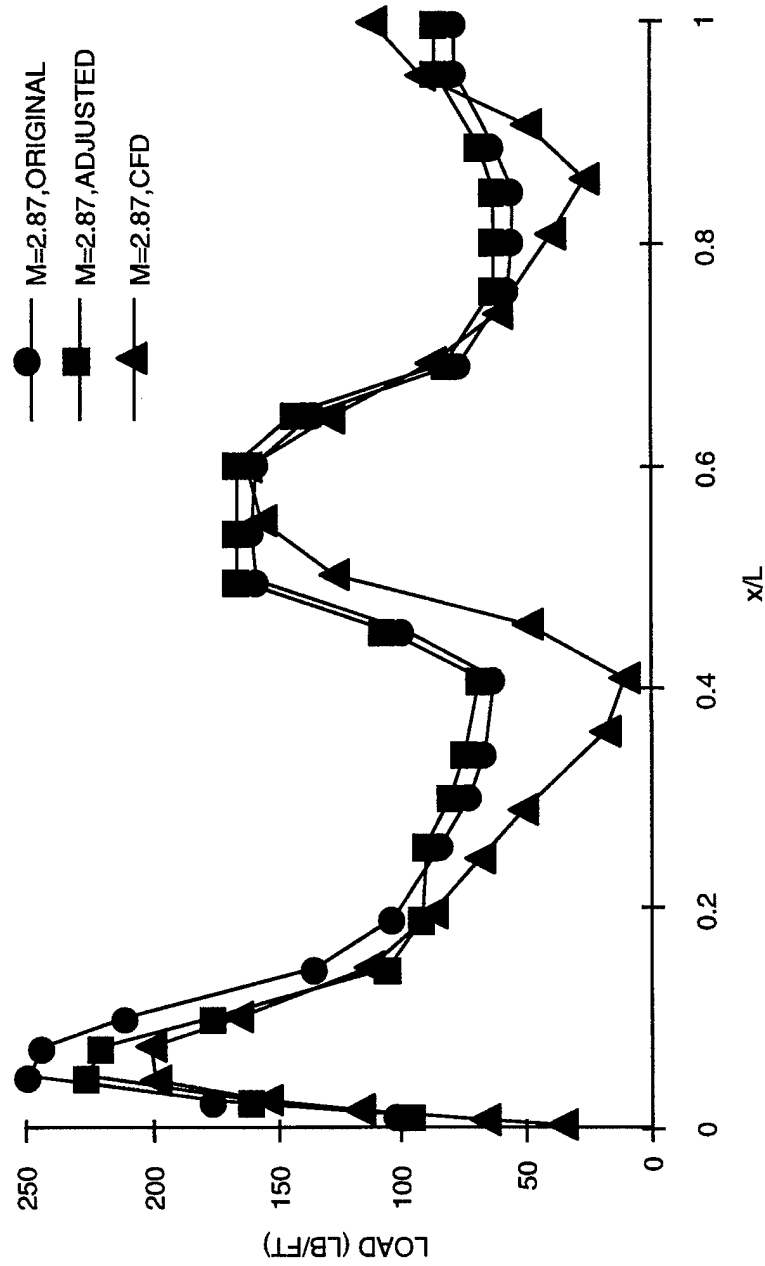


FIGURE 1. EFFECT OF ADJUSTMENT OF NONLINEAR COMPONENT OF NOSE LOAD

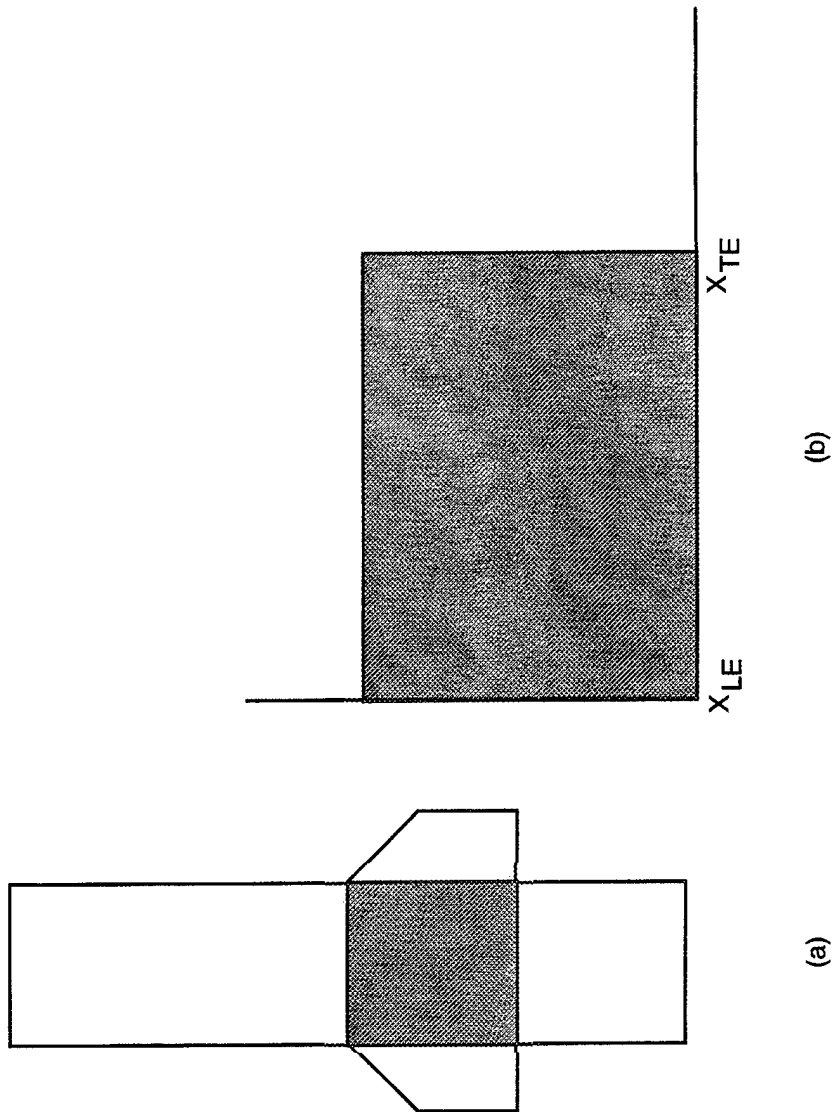


FIGURE 2. DISTRIBUTION OF UNIFORM BODY-WING INTERFERENCE LOADS

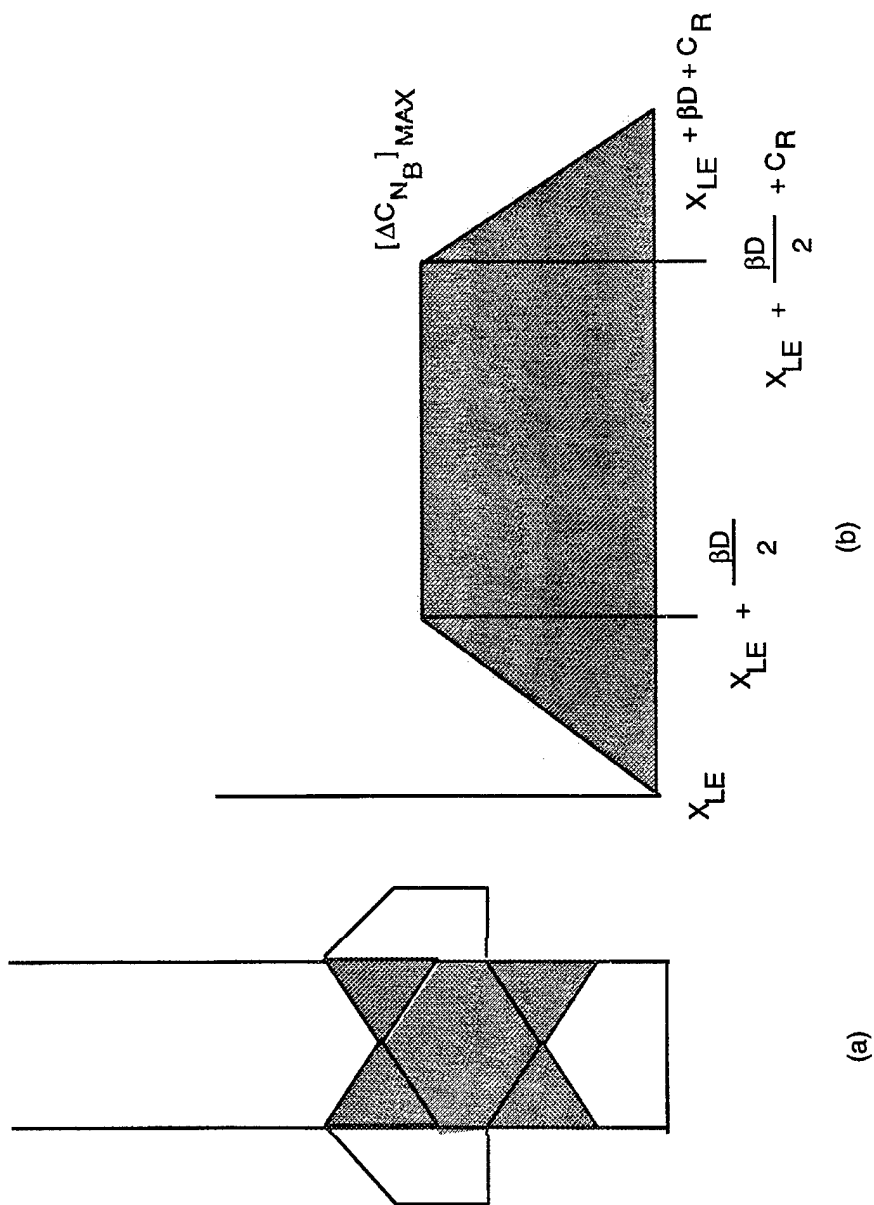


FIGURE 3. DISTRIBUTION OF TRAPEZOIDAL BODY-WING INTERFERENCE LOADS

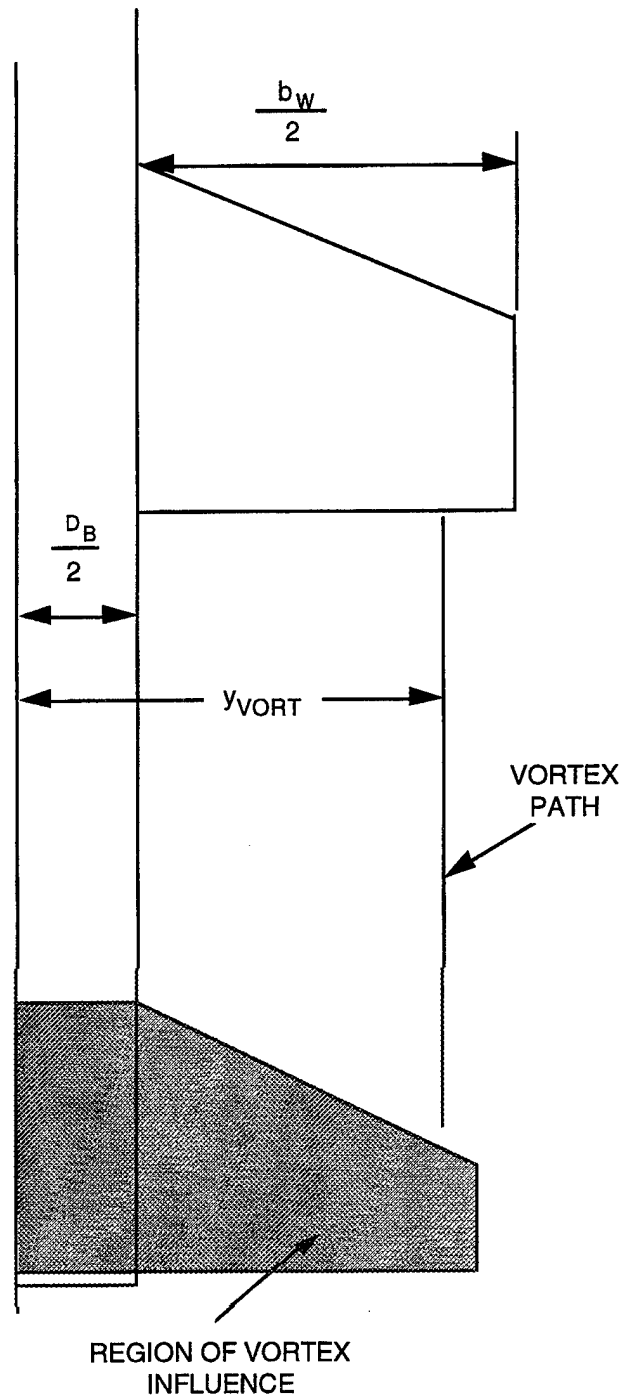


FIGURE 4. GEOMETRY OF WING-TAIL INTERFERENCE DISTRIBUTION MODEL

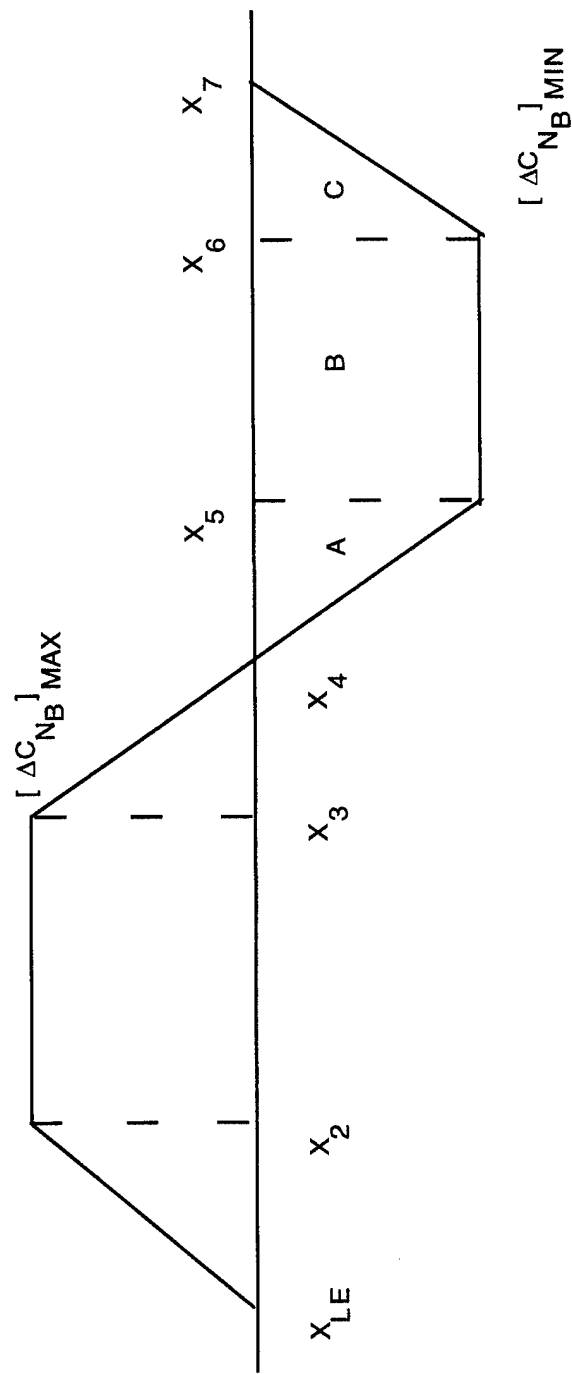


FIGURE 5. DISTRIBUTION OF NEGATIVE COMPONENT OF BODY-WING INTERFERENCE LOADS

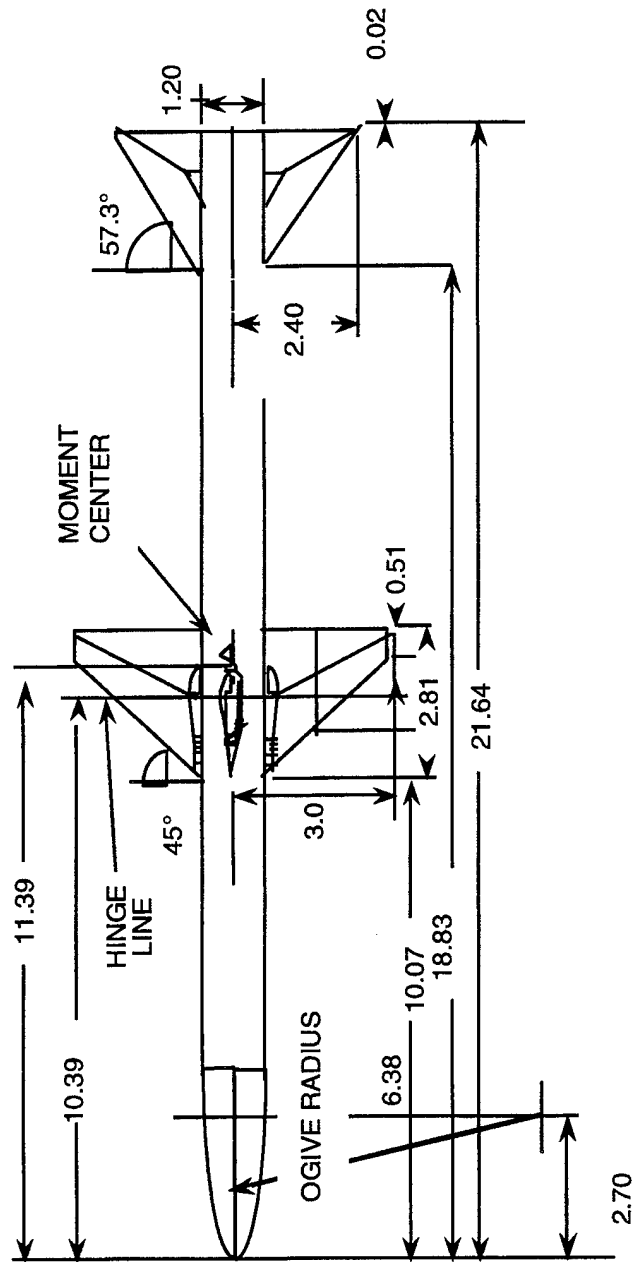


FIGURE 6. SEASPARROW MISSILE

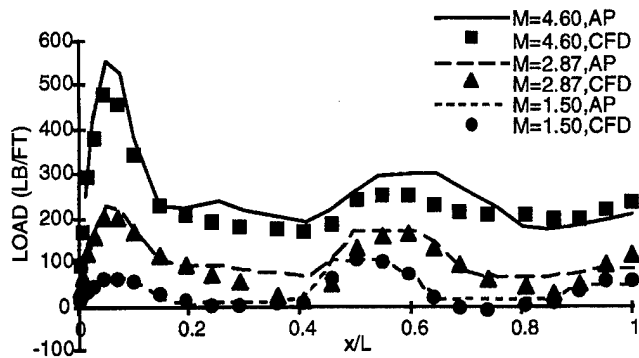
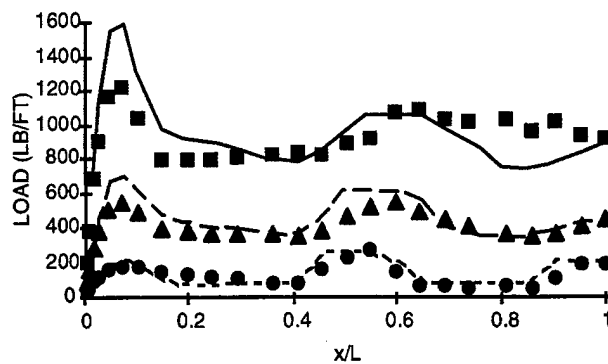
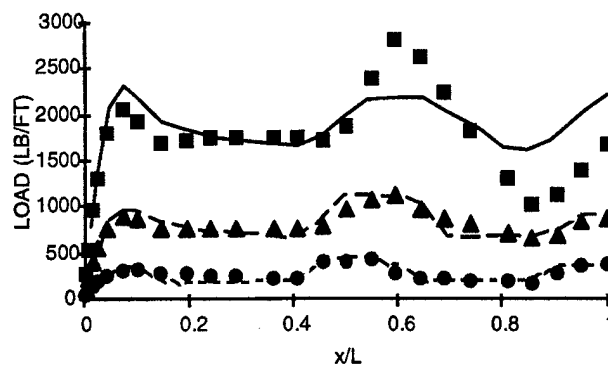
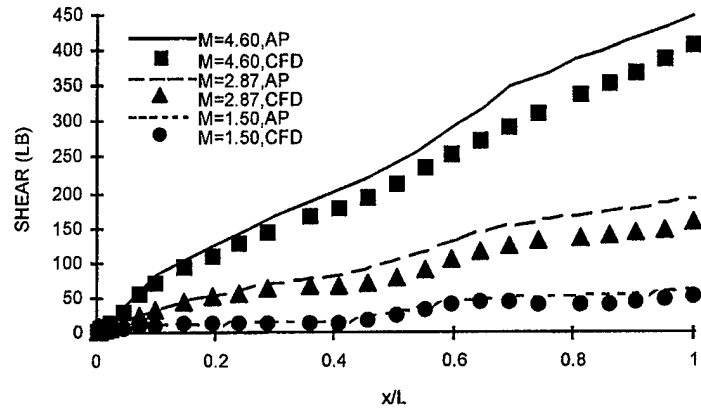
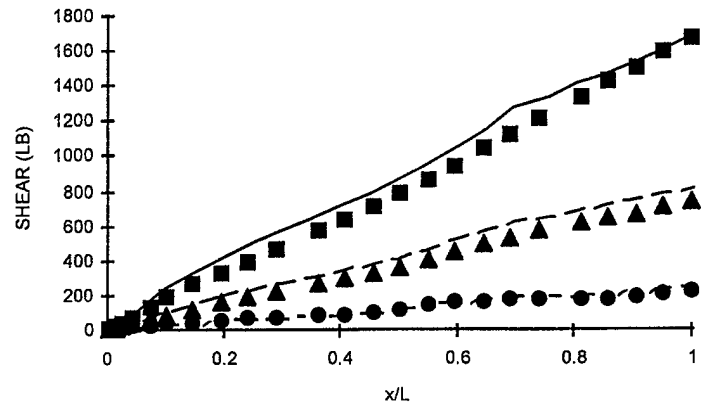
(a) $\alpha = 10^\circ$ (b) $\alpha = 25^\circ$ (c) $\alpha = 40^\circ$

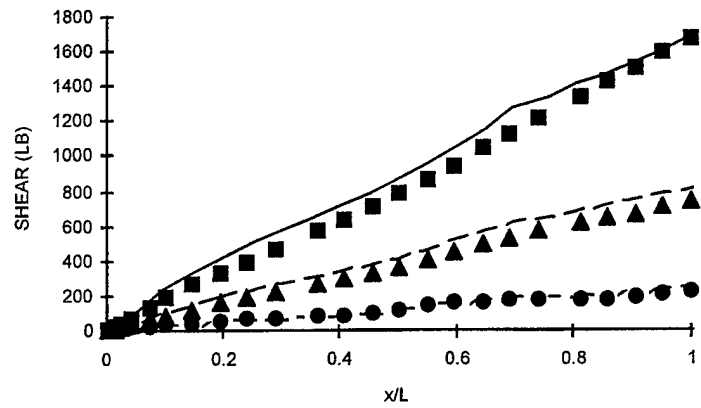
FIGURE 7. BODY LOADING AT $\Phi = 0^\circ$: (a) ALPHA = 10° ,
(b) ALPHA = 25° , AND (c) ALPHA = 40°



(a) $\alpha = 10^\circ$



(b) $\alpha = 25^\circ$



(c) $\alpha = 40^\circ$

FIGURE 8. BODY SHEAR AT $\Phi = 0^\circ$: (a) ALPHA = 10° ,
(b) ALPHA = 25° , AND (c) ALPHA = 40°

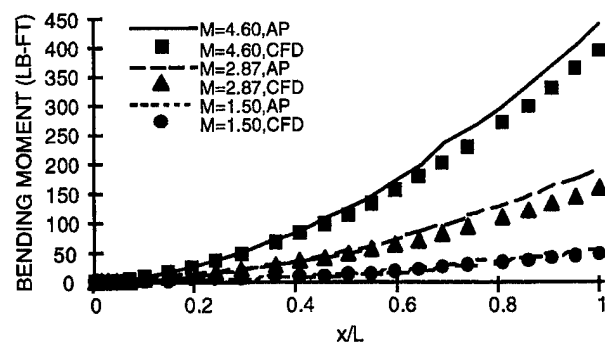
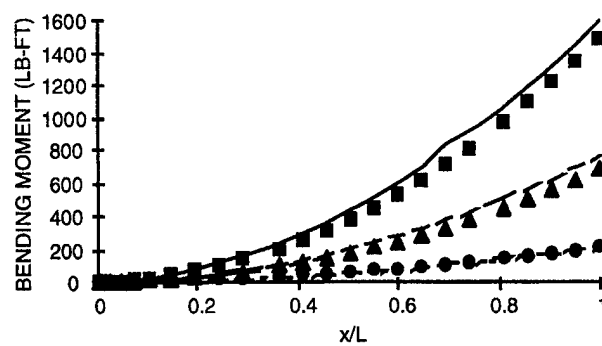
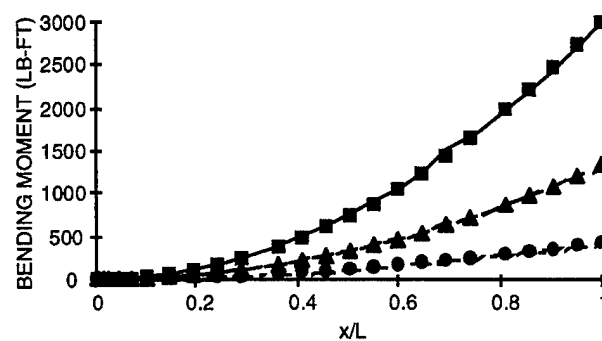
(a) $\alpha = 10^\circ$ (b) $\alpha = 25^\circ$ (c) $\alpha = 40^\circ$

FIGURE 9. BODY BENDING MOMENT AT $\Phi = 0^\circ$: (a) ALPHA = 10° ,
(b) ALPHA = 25° , AND (c) ALPHA = 40°

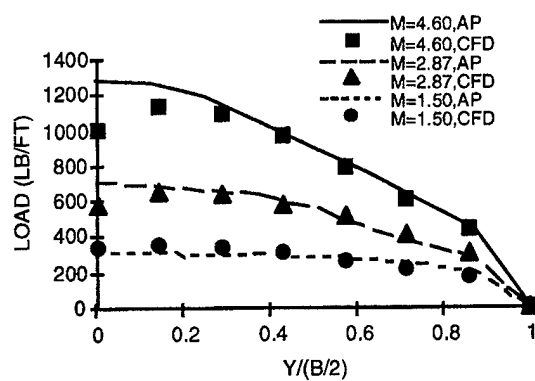
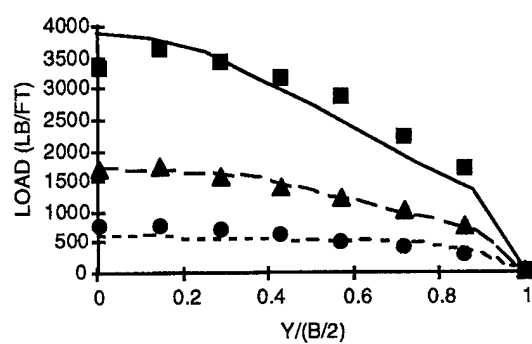
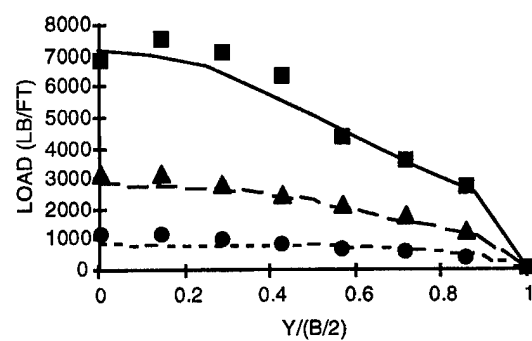
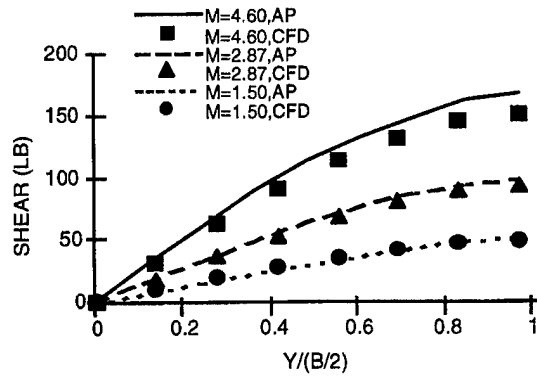
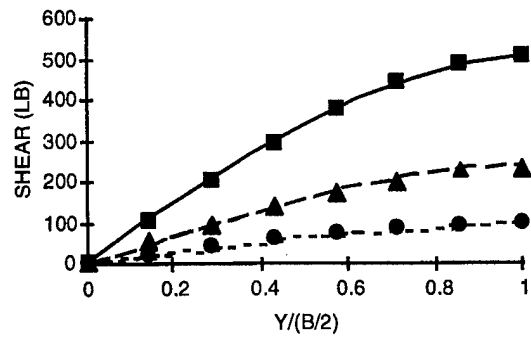
(a) $\alpha = 10^\circ$ (b) $\alpha = 25^\circ$ (c) $\alpha = 40^\circ$

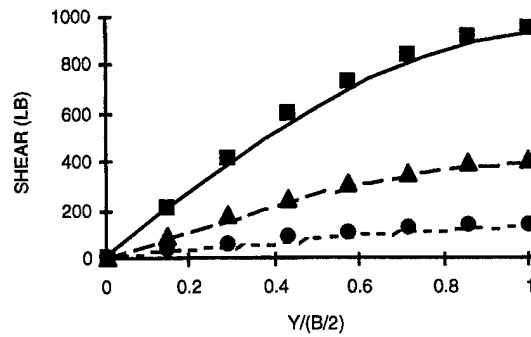
FIGURE 10. WING LOADING AT $\Phi = 0^\circ$: (a) ALPHA = 10° ,
(b) ALPHA = 25° , AND (c) ALPHA = 40°



(a) $\alpha = 10^\circ$



(b) $\alpha = 25^\circ$



(c) $\alpha = 40^\circ$

FIGURE 11. WING SHEAR AT $\Phi = 0^\circ$: (a) ALPHA = 10° ,
(b) ALPHA = 25° , AND (c) ALPHA = 40°

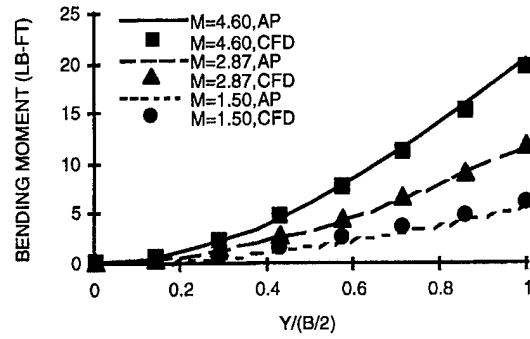
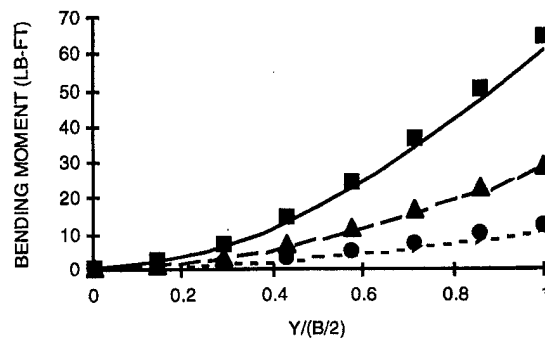
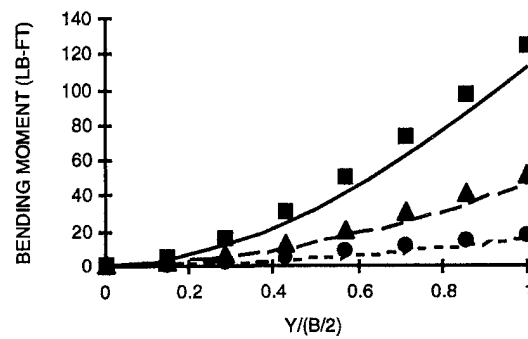
(a) $\alpha = 10^\circ$ (b) $\alpha = 25^\circ$ (c) $\alpha = 40^\circ$

FIGURE 12. WING BENDING MOMENT AT $\Phi = 0^\circ$: (a) ALPHA = 10° ,
(b) ALPHA = 25° , AND (c) ALPHA = 40°

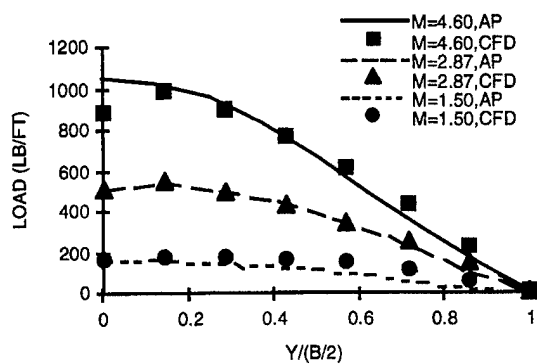
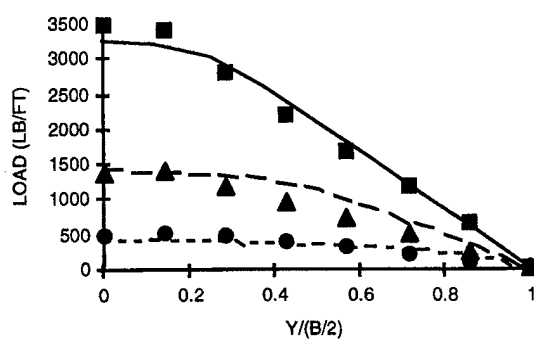
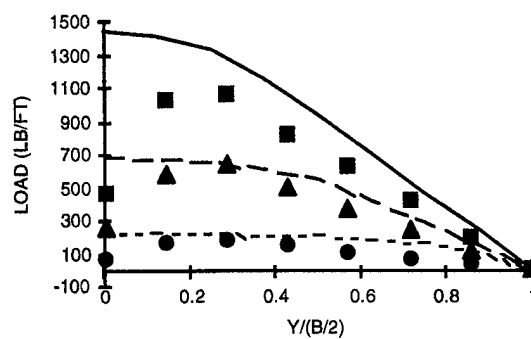
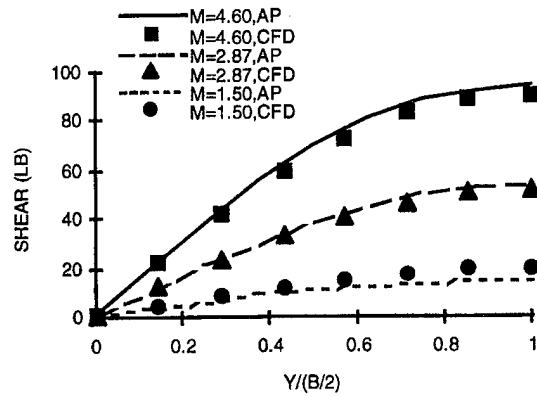
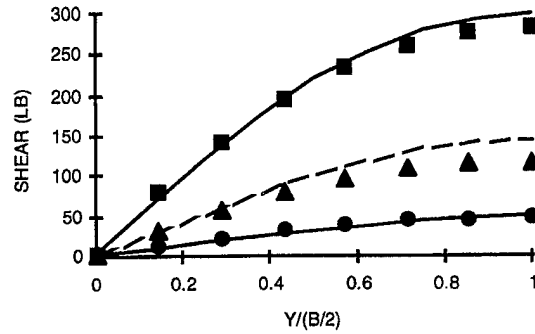
(a) $\alpha = 10^\circ$ (b) $\alpha = 25^\circ$ (c) $\alpha = 40^\circ$

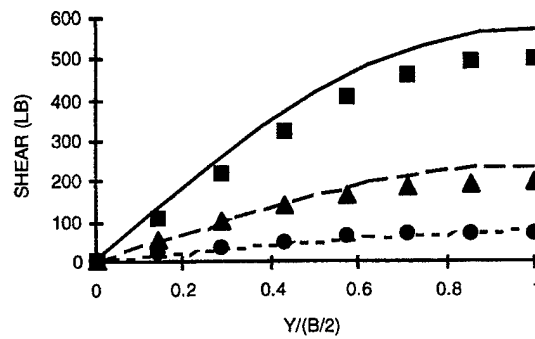
FIGURE 13. TAIL LOADING AT $\Phi = 0^\circ$: (a) ALPHA = 10° ,
(b) ALPHA = 25° , AND (c) ALPHA = 40°



(a) $\alpha = 10^\circ$



(b) $\alpha = 25^\circ$



(c) $\alpha = 40^\circ$

FIGURE 14. TAIL SHEAR AT $\Phi = 0^\circ$: (a) ALPHA = 10° ,
(b) ALPHA = 25° , AND (c) ALPHA = 40°

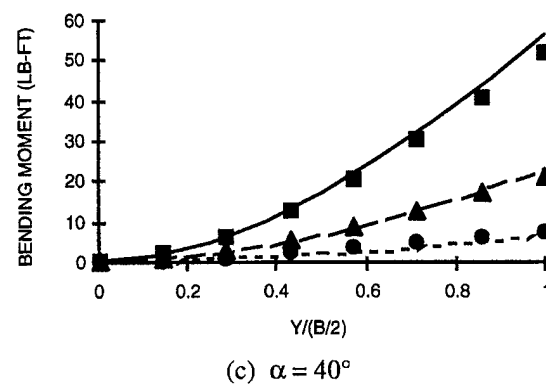
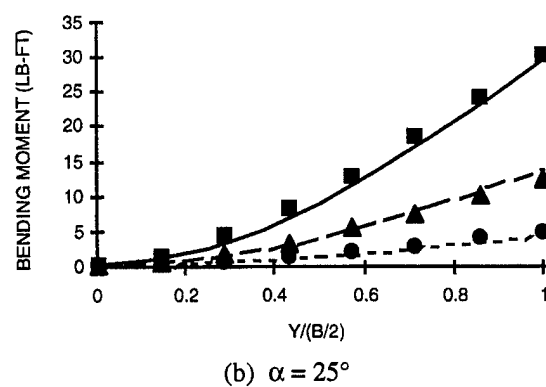
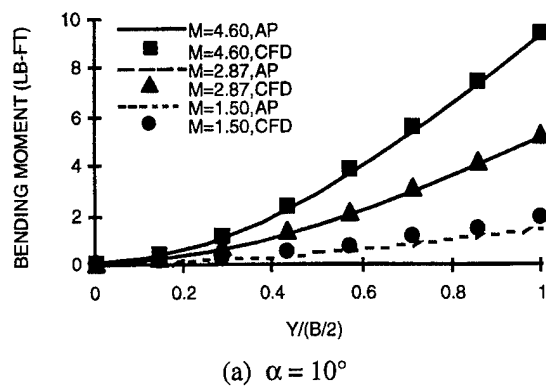


FIGURE 15. TAIL BENDING MOMENT AT $\Phi = 0^\circ$: (a) ALPHA = 10° , (b) ALPHA = 25° , AND (c) ALPHA = 40°

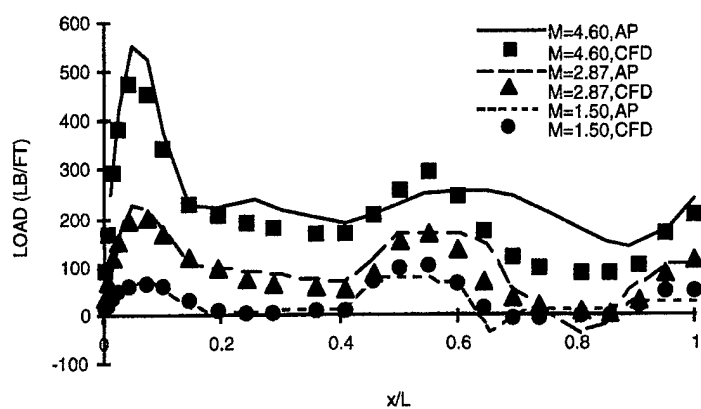
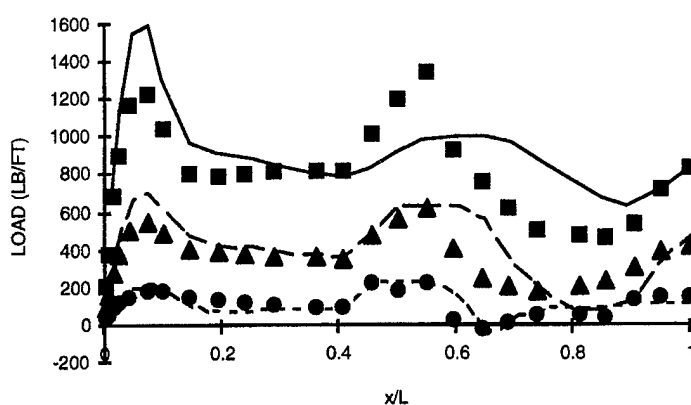
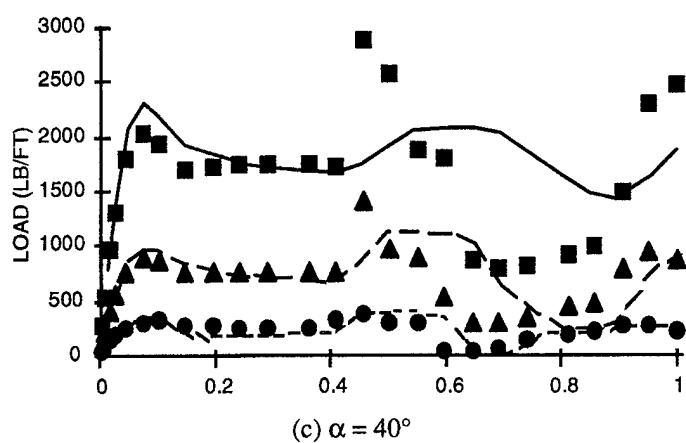
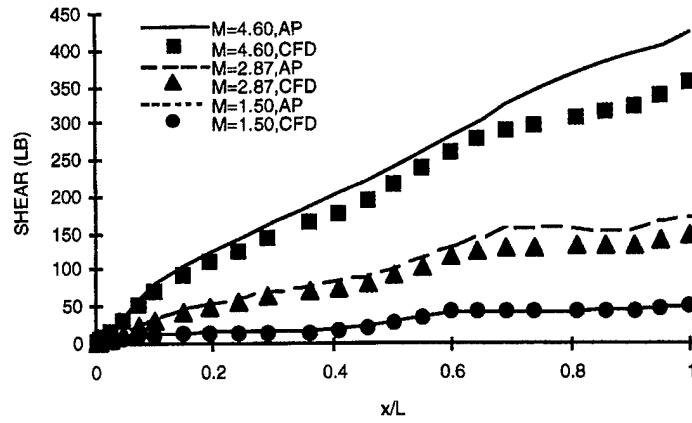
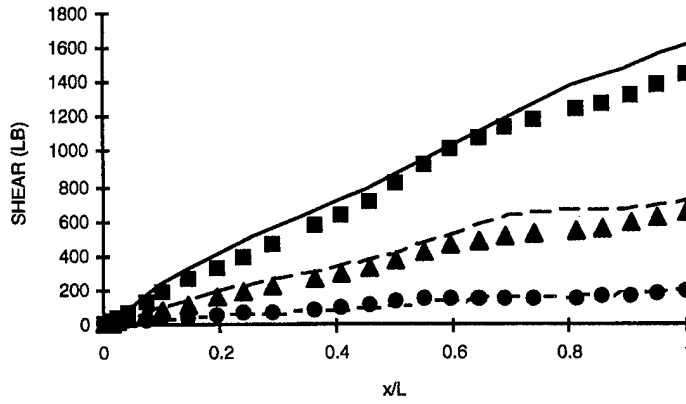
(a) $\alpha = 10^\circ$ (b) $\alpha = 25^\circ$ (c) $\alpha = 40^\circ$

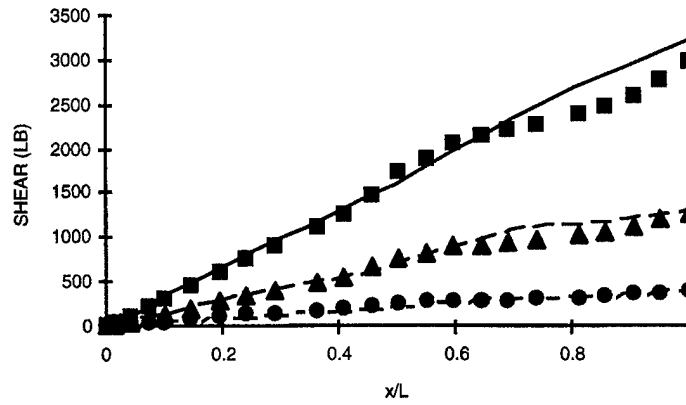
FIGURE 16. BODY LOADING AT $\Phi = 45^\circ$: (a) ALPHA = 10° ,
(b) ALPHA = 25° , AND (c) ALPHA = 40°



(a) $\alpha = 10^\circ$



(b) $\alpha = 25^\circ$



(c) $\alpha = 40^\circ$

FIGURE 17. BODY SHEAR AT $\Phi = 45^\circ$: (a) ALPHA = 10° , (b) ALPHA = 25° , AND (c) ALPHA = 40°

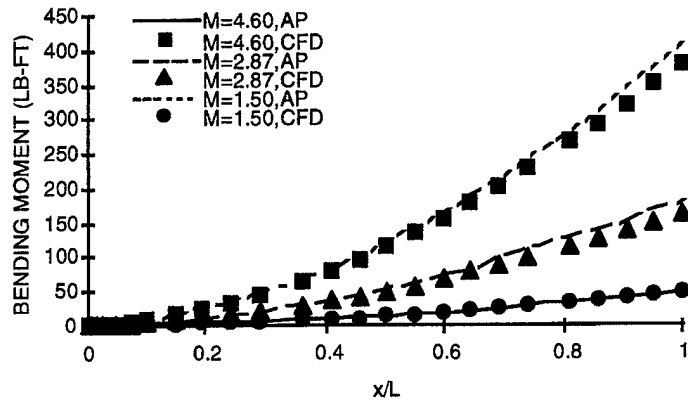
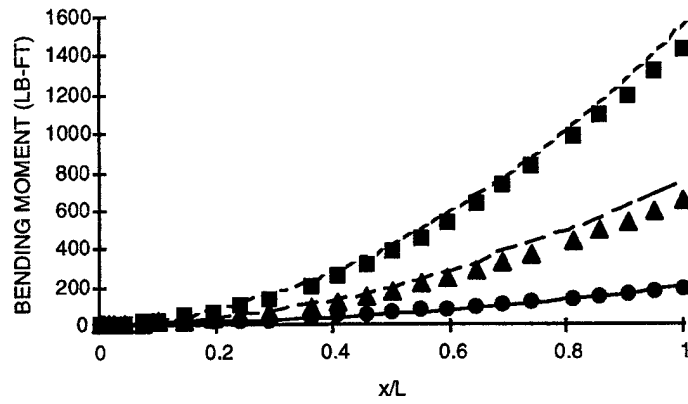
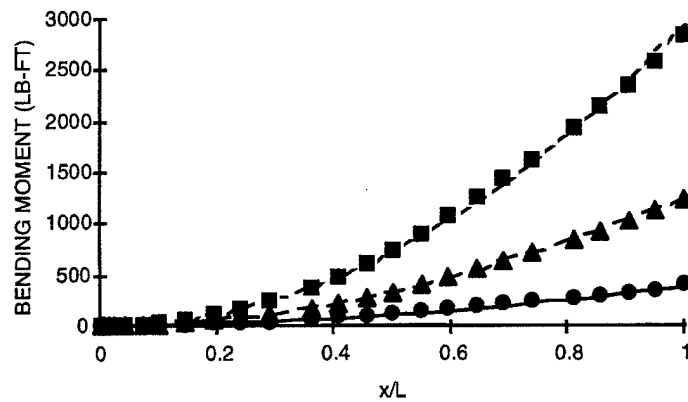
(a) $\alpha = 10^\circ$ (b) $\alpha = 25^\circ$ (c) $\alpha = 40^\circ$

FIGURE 18. BODY BENDING MOMENT AT $\Phi = 45^\circ$: (a) ALPHA = 10° ,
(b) ALPHA = 25° , AND (c) ALPHA = 40°

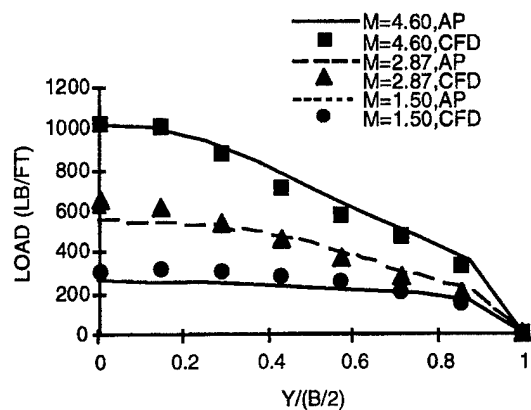
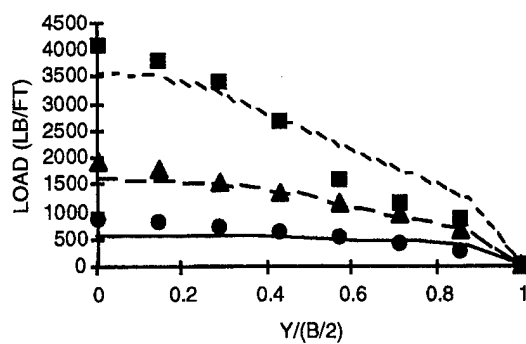
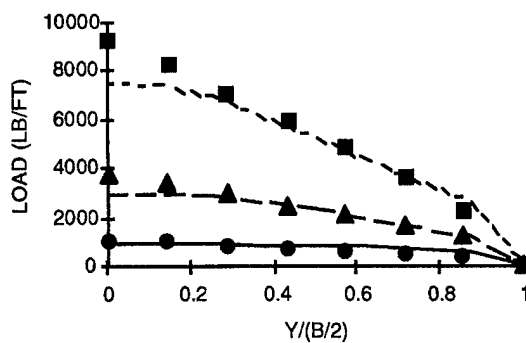
(a) $\alpha = 10^\circ$ (b) $\alpha = 25^\circ$ (c) $\alpha = 40^\circ$

FIGURE 19. WINDWARD WING LOADING AT $\Phi = 45^\circ$: (a) ALPHA = 10° ,
(b) ALPHA = 25° , AND (c) ALPHA = 40°

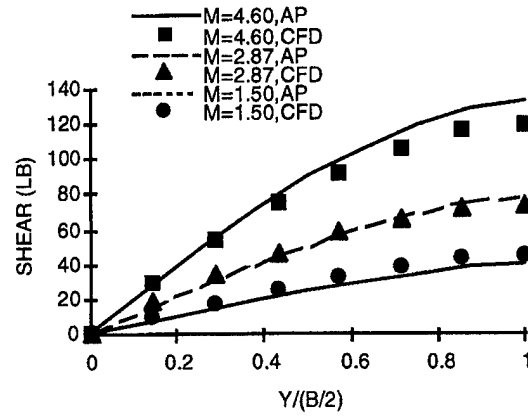
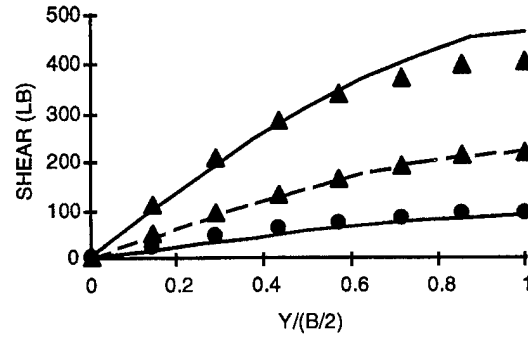
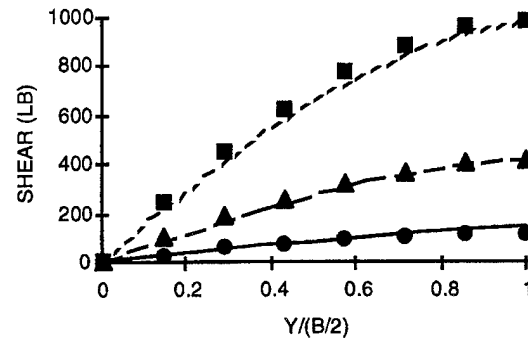
(a) $\alpha = 10^\circ$ (b) $\alpha = 25^\circ$ (c) $\alpha = 40^\circ$

FIGURE 20. WINDWARD WING SHEAR AT $\Phi = 45^\circ$: (a) ALPHA = 10° ,
(b) ALPHA = 25° , AND (c) ALPHA = 40°

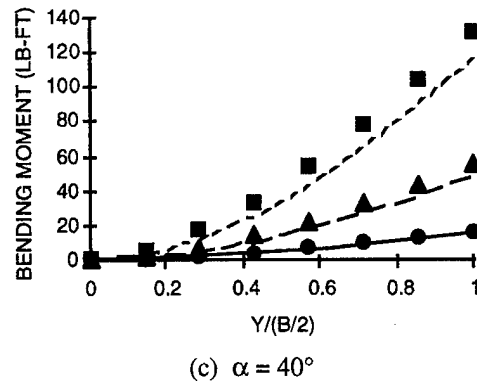
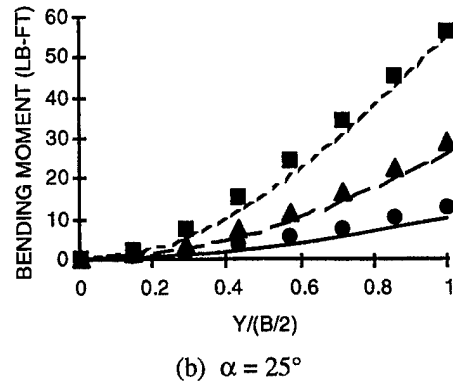
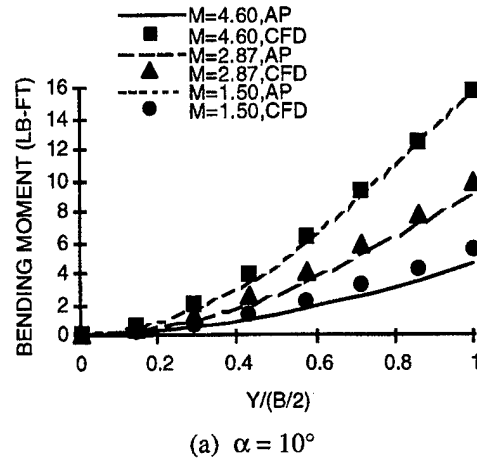


FIGURE 21. WINDWARD WING BENDING MOMENT AT $\Phi = 45^\circ$: (a) ALPHA = 10° ,
(b) ALPHA = 25° , AND (c) ALPHA = 40°

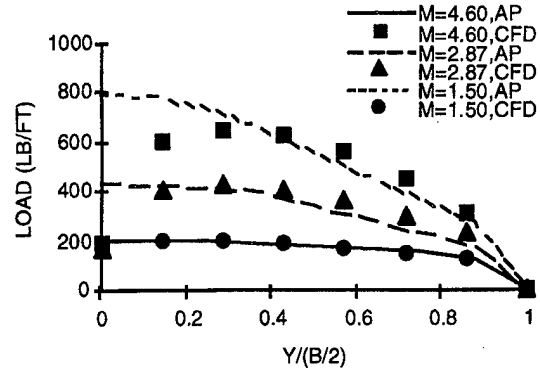
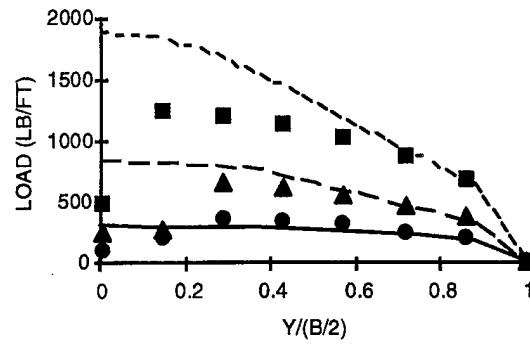
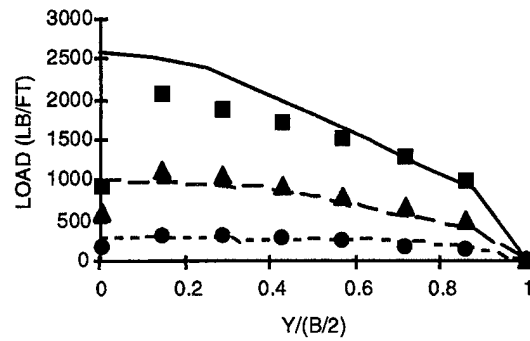
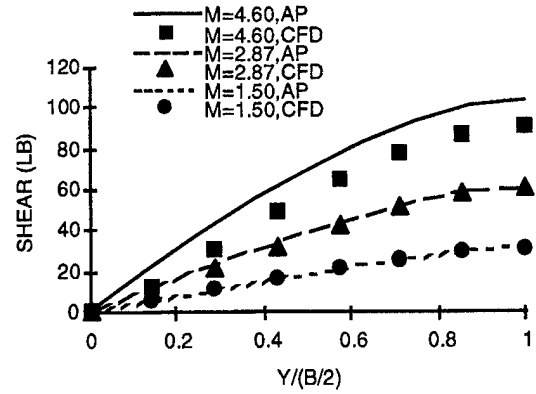
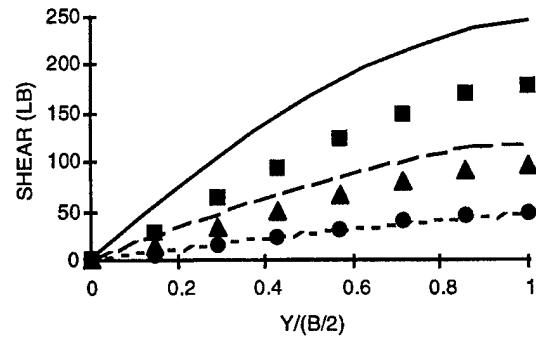
(a) $\alpha = 10^\circ$ (b) $\alpha = 25^\circ$ (c) $\alpha = 40^\circ$

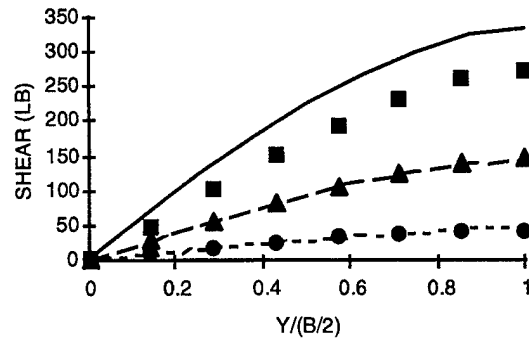
FIGURE 22. LEEWARD WING LOADING AT $\Phi = 45^\circ$: (a) ALPHA = 10° ,
(b) ALPHA = 25° , AND (c) ALPHA = 40°



(a) $\alpha = 10^\circ$



(b) $\alpha = 25^\circ$



(c) $\alpha = 40^\circ$

FIGURE 23. LEEWARD WING SHEAR AT $\Phi = 45^\circ$: (a) ALPHA = 10° , (b) ALPHA = 25° , AND (c) ALPHA = 40°

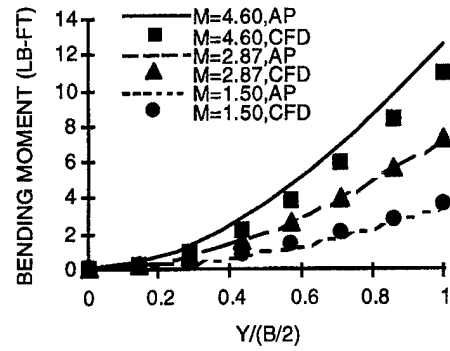
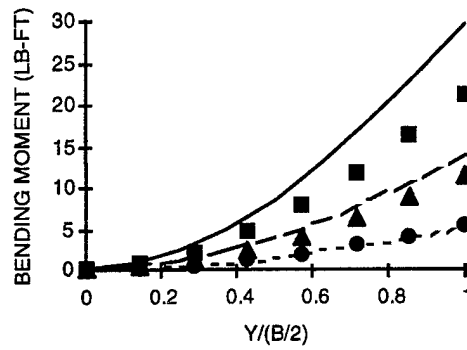
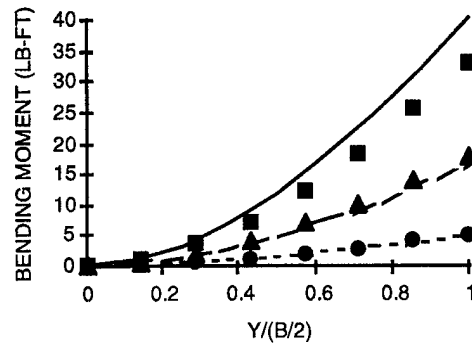
(a) $\alpha = 10^\circ$ (b) $\alpha = 25^\circ$ (c) $\alpha = 40^\circ$

FIGURE 24. LEEWARD WING BENDING MOMENT AT $\Phi = 45^\circ$: (a) ALPHA = 10° ,
(b) ALPHA = 25° , AND (c) ALPHA = 40°

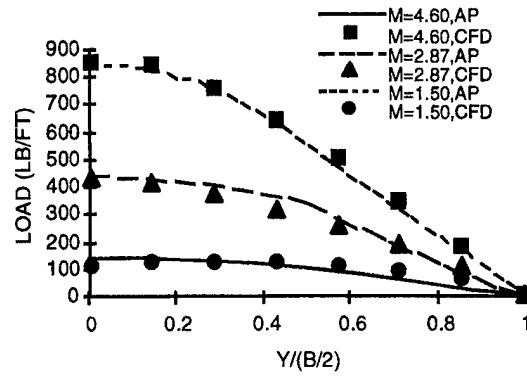
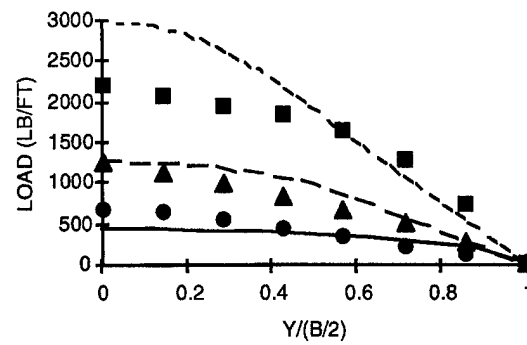
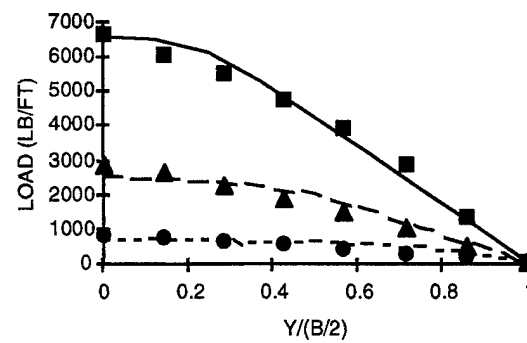
(a) $\alpha = 10^\circ$ (b) $\alpha = 25^\circ$ (c) $\alpha = 40^\circ$

FIGURE 25. WINDWARD TAIL LOADING AT $\Phi = 45^\circ$: (a) ALPHA = 10° ,
(b) ALPHA = 25° , AND (c) ALPHA = 40°

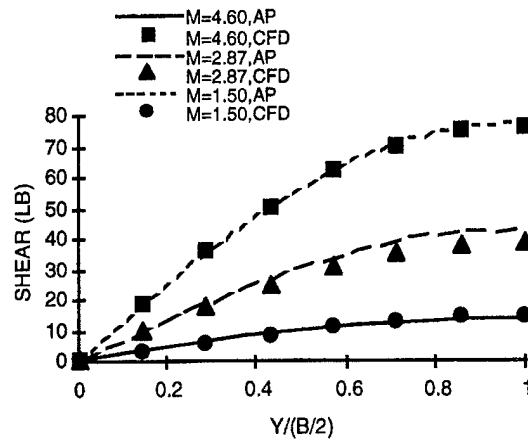
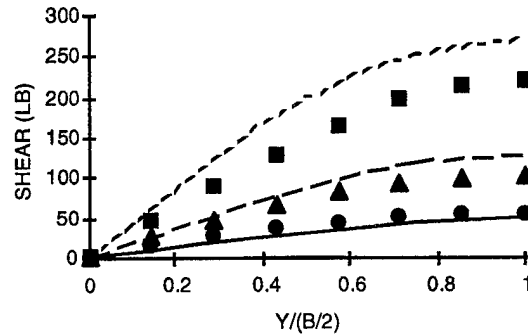
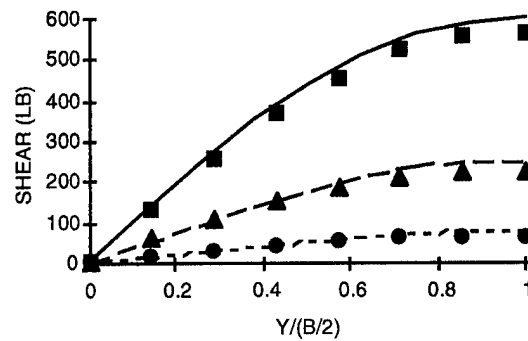
(a) $\alpha = 10^\circ$ (b) $\alpha = 25^\circ$ (c) $\alpha = 40^\circ$

FIGURE 26. WINDWARD TAIL SHEAR AT $\Phi = 45^\circ$: (a) ALPHA = 10° ,
(b) ALPHA = 25° , AND (c) ALPHA = 40°

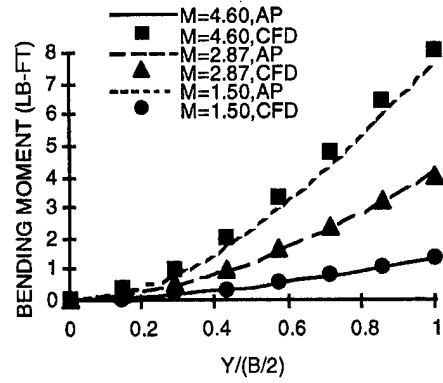
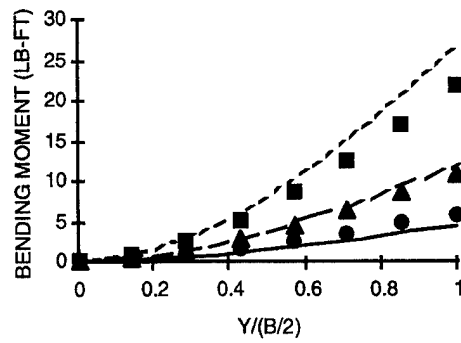
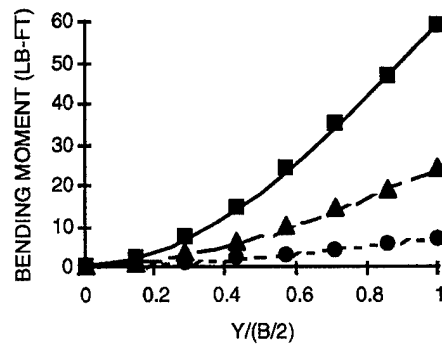
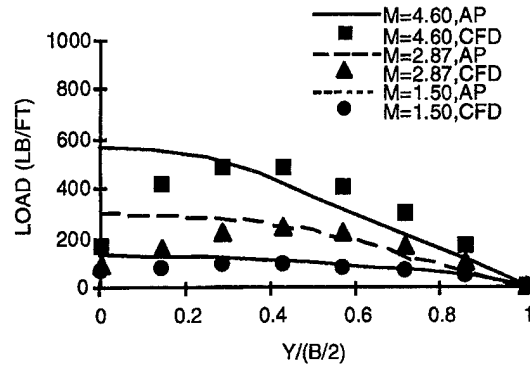
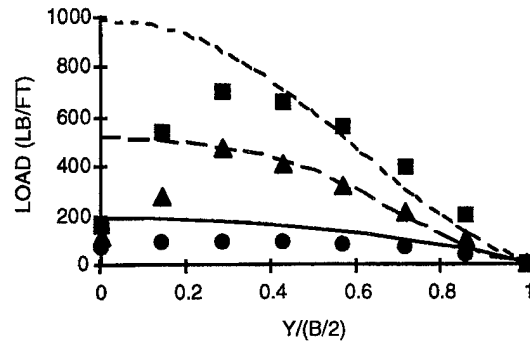
(a) $\alpha = 10^\circ$ (b) $\alpha = 25^\circ$ (c) $\alpha = 40^\circ$

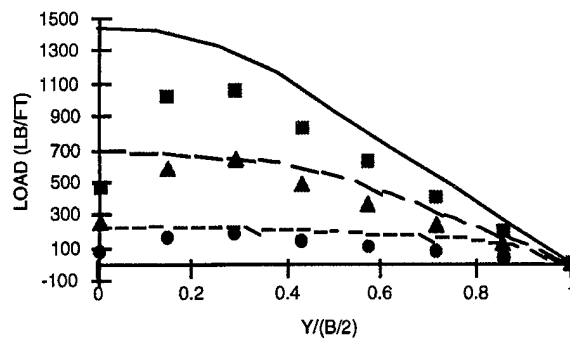
FIGURE 27. WINDWARD TAIL BENDING MOMENT AT $\Phi = 45^\circ$: (a) ALPHA = 10° , (b) ALPHA = 25° , AND (c) ALPHA = 40°



(a) $\alpha = 10^\circ$



(b) $\alpha = 25^\circ$



(c) $\alpha = 40^\circ$

FIGURE 28. LEEWARD TAIL LOADING AT $\Phi = 45^\circ$: (a) ALPHA = 10° , (b) ALPHA = 25° , AND (c) ALPHA = 40°

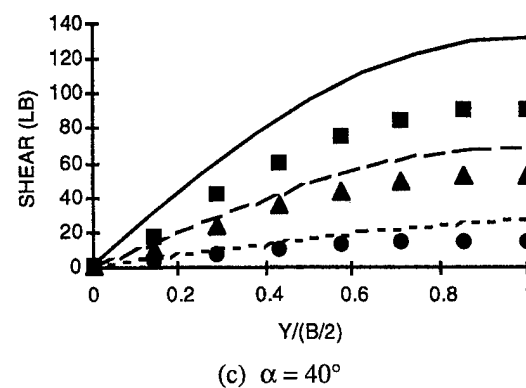
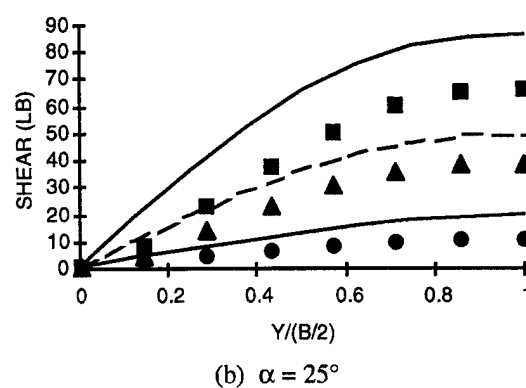
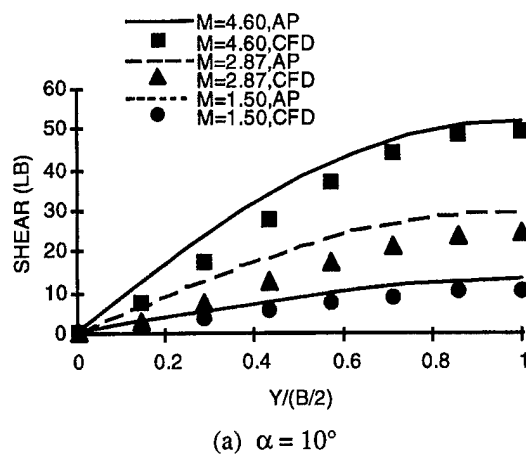


FIGURE 29. LEEWARD TAIL SHEAR AT $\Phi = 45^\circ$: (a) ALPHA = 10° ,
(b) ALPHA = 25° , AND (c) ALPHA = 40°

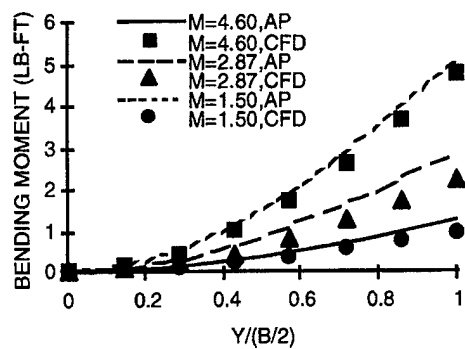
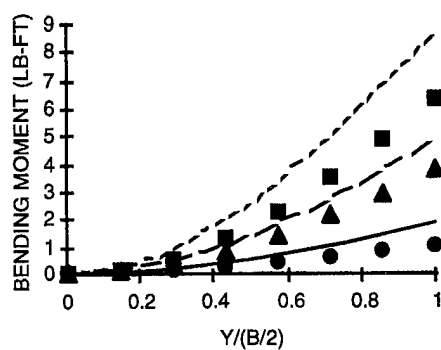
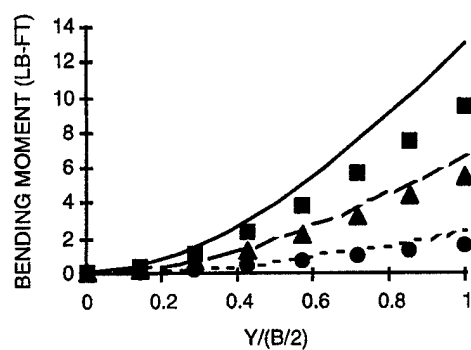
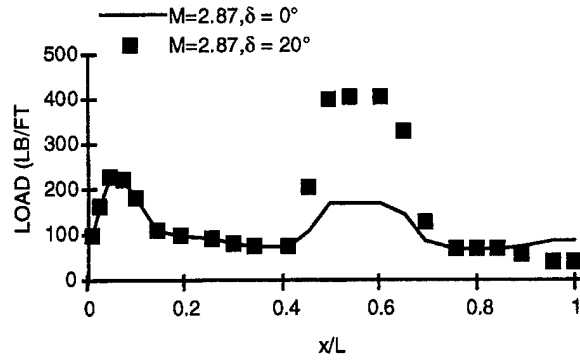
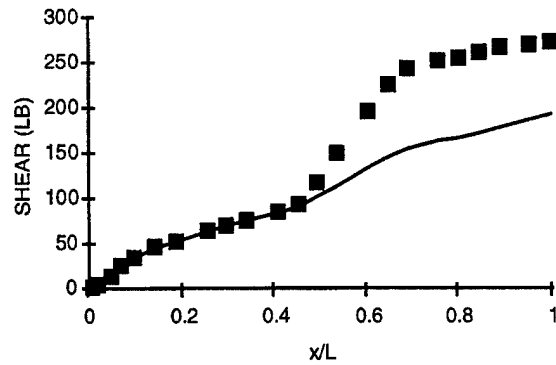
(a) $\alpha = 10^\circ$ (b) $\alpha = 25^\circ$ (c) $\alpha = 40^\circ$

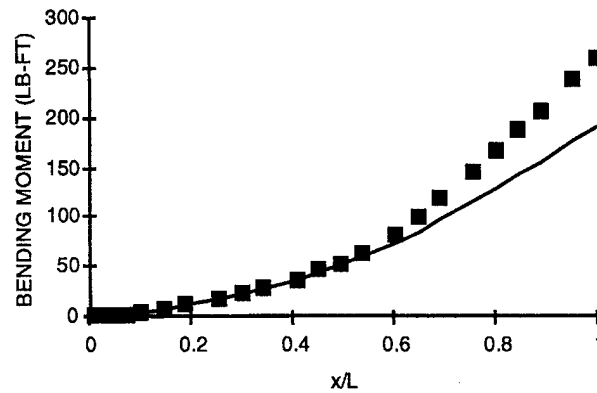
FIGURE 30. LEEWARD TAIL BENDING MOMENT AT $\Phi = 45^\circ$: (a) ALPHA = 10° ,
(b) ALPHA = 25° , AND (c) ALPHA = 40°



(a) BODY LOADING

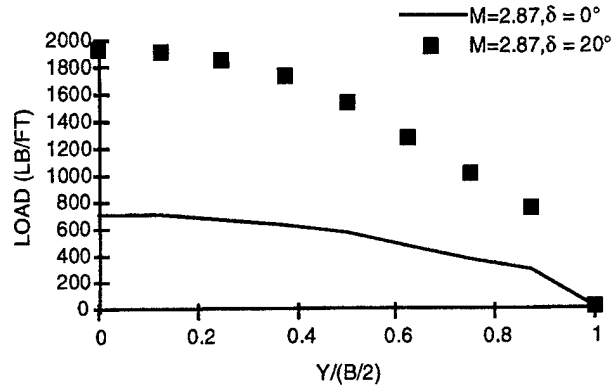


(b) BODY SHEAR

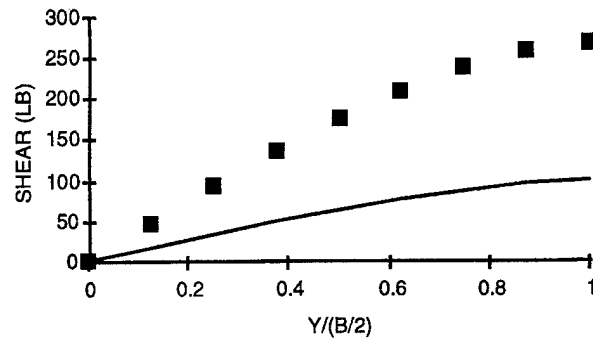


(c) BODY BENDING MOMENT

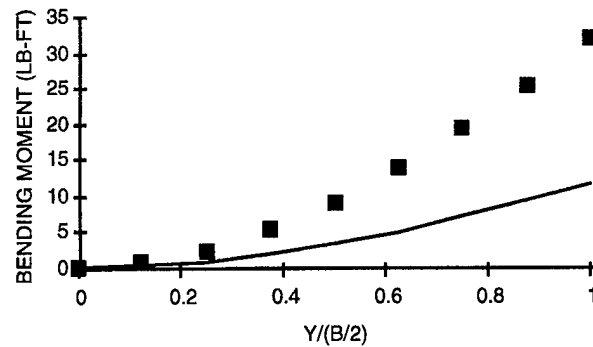
FIGURE 31. EFFECT OF WING DEFLECTION AT
 $\alpha = 10^\circ, \Phi = 0^\circ$: (a) BODY LOADING, (b) BODY SHEAR,
 AND (c) BODY BENDING MOMENT



(a) WING LOADING

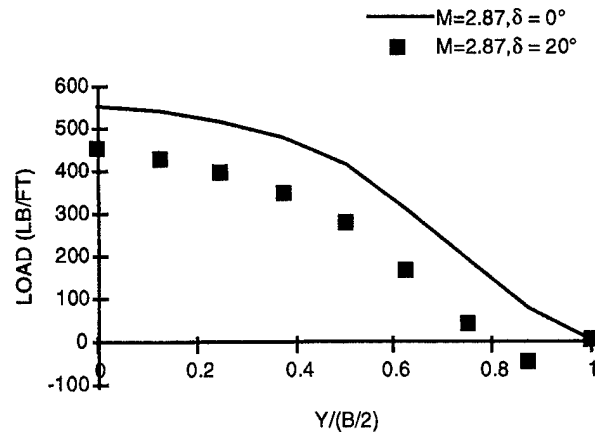


(b) WING SHEAR

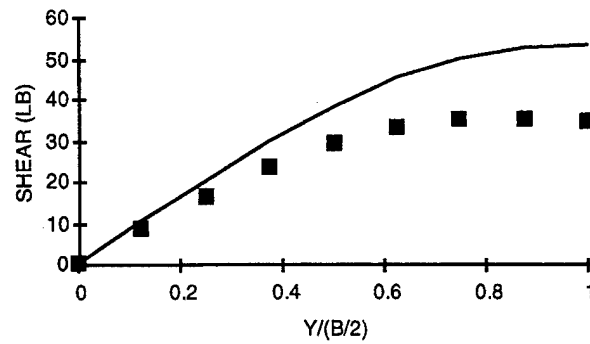


(c) WING BENDING MOMENT

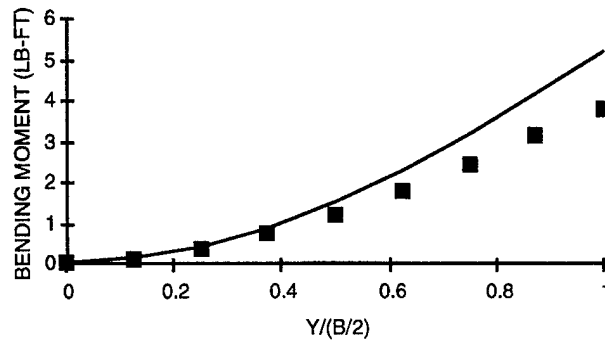
FIGURE 32. EFFECT OF WING DEFLECTION AT $\alpha = 10^\circ$, $\Phi = 0^\circ$: (a) WING LOADING, (b) WING SHEAR, AND (c) WING BENDING MOMENT



(a) TAIL LOADING



(b) TAIL SHEAR



(c) TAIL BENDING MOMENT

FIGURE 33. EFFECT OF WING DEFLECTION AT $\alpha = 10^\circ$, $\Phi = 0^\circ$: (a) TAIL LOADING, (b) TAIL SHEAR, AND (c) TAIL BENDING MOMENT

DISTRIBUTION

	<u>Copies</u>		<u>Copies</u>
DOD ACTIVITIES (CONUS)		ATTN C KLEIN	1
		TECHNICAL LIBRARY	1
ATTN CODE 04 (BISSON)	1	COMMANDER	
CODE 30	1	NAVAL AIR WARFARE CENTER	
CODE 44 (ZIMET)	1	WEAPONS DIVISION	
CODE 4425 (SIEGEL)	1	521 9TH ST	
CODE 332FD (LEKOU DIS)	1	POINT MUGU CA 93042-5001	
CODE 442 (WOOD)	1		
CHIEF OF NAVAL RESEARCH		ATTN T C TAI	1
BALLSTON CENTRE TOWER ONE		M J MALIA	1
800 NORTH QUINCY ST		TECHNICAL LIBRARY	1
ARLINGTON VA 22217-5660		COMMANDER	
		NAVAL SHIP RESEARCH AND	
ATTN CODE 474T6OD (LOFTUS)	1	DEVELOPMENT CENTER	
CODE 4732HOD (SMITH)	1	WASHINGTON DC 20034	
CODE 473COOB (PORTER)	1		
CODE 47311OD (HOUSH)	5	ATTN R M HOWARD	1
CODE 47311OD (GLEASON)	1	TECHNICAL LIBRARY	1
CODE 47311OD (VAN DYKEN)	1	SUPERINTENDENT	
CODE 4722EOD (JETER)	1	NAVAL POSTGRADUATE SCHOOL	
TECHNICAL LIBRARY	1	1 UNIVERSITY CIRCLE	
COMMANDER		MONTEREY CA 93943-5001	
NAVAL AIR WARFARE CENTER			
WEAPONS DIVISION		ATTN S GREENHALGH	1
1 ADMINISTRATION CIRCLE		C REITZ	1
CHINA LAKE CA 93555-6001		TECHNICAL LIBRARY	1
		COMMANDING OFFICER	
ATTN TECHNICAL LIBRARY	1	NAVAL AIR WARFARE CENTER	
COMMANDER		AIRCRAFT DIVISION WARMINSTER	
NAVAL SEA SYSTEMS COMMAND		BOX 5152	
2531 JEFFERSON DAVIS HWY		WARMINSTER PA 18974-0591	
ARLINGTON VA 22242-5160			
		ATTN HEAD WEAPONS DEPT	1
ATTN AIR 53012D (JOHNSON)	1	HEAD SCIENCE DEPT	1
RM 904 JP 2		SUPERINTENDENT	
TECHNICAL LIBRARY	1	UNITED STATES NAVAL ACADEMY	
COMMANDER		121 BLAKE RD	
NAVAL AIR SYSTEMS COMMAND		ANNAPOLIS MD 21402-5000	
HEADQUARTERS			
1421 JEFFERSON DAVIS HWY		ATTN M KRUMINS	1
ARLINGTON VA 22243-5120		TECHNICAL LIBRARY	1
		OFFICER IN CHARGE	
		NAVAL INTELLIGENCE SUPPORT CENTER	
		4301 SUITLAND ROAD	
		ALEXANDRIA VA 22217	

DISTRIBUTION (Continued)

	<u>Copies</u>		<u>Copies</u>
ATTN DIAG DT 4T (PAUL MURAD)	2	ATTN B BLAKE (BLD 146)	1
DIRECTOR		D SHEREDA (BLD 450)	1
DEFENSE INTELLIGENCE AGENCY		J JENKINS (BLD 146)	1
WASHINGTON DC 20301		R SAMUELS (BLD 856)	1
		TECHNICAL LIBRARY	1
ATTN BRENT WAGGONER	1	COMMANDING OFFICER	
CODE 4072 BLDG 2540		AFSC	
NAVAL WEAPONS SUPPORT CENTER		2210 8TH STREET	
CRANE IN 47522-5000		WRIGHT PATTERSON AFB OH 45433	
ATTN CODE 5252P (KRAUSE)	1	ATTN J USSELTON	1
TECHNICAL LIBRARY	1	W B BAKER JR	1
COMMANDER		TECHNICAL LIBRARY	1
INDIAN HEAD DIVISION		ARNOLD ENGINEERING DEVELOPMENT	
NAVAL SURFACE WARFARE CENTER		CENTER USAF	
101 STRAUSS AVE		TULLAHOMA TN 37389	
INDIAN HEAD MD 20640-5035			
ATTN TECHNICAL LIBRARY	1	ATTN H HUDGINS	1
COMMANDING GENERAL		G FRIEDMAN	1
MARINE CORPS COMBAT		TECHNICAL LIBRARY	1
DEVELOPMENT COMMAND		COMMANDING GENERAL	
2048 SOUTH ST		ARRADCOM PICATINNY ARSENAL	
QUANTICO VA 22134-5129		DOVER NJ 07801	
ATTN E SEARS	1	ATTN C H MURPHY	1
L E LIJEWSKI	1	R PUHALLA JR	1
C COTTRELL	1	W STUREK	1
TECHNICAL LIBRARY	1	C NIETUBICZ	1
AFATL (ADLRA) (DLGC)	1	A MIKHAIL	1
EGLIN AFB FL 32542-5000		P PLOSTINS	1
		TECHNICAL LIBRARY	1
ATTN TECHNICAL LIBRARY	1	COMMANDING GENERAL	
USAF ACADEMY		BALLISTIC RESEARCH LABORATORY	
COLORADO SPRINGS CO 80912		ABERDEEN PROVING GROUND	
		ABERDEEN MD 21005-5066	
ATTN TECHNICAL LIBRARY	1	ATTN CODE TNC (BLACKLEDGE)	1
ADVANCED RESEARCH PROJECTS		RICH MATLOCK	1
AGENCY		DIRECTOR	
DEPARTMENT OF DEFENSE		INTERCEPTOR TECHNOLOGY	
WASHINGTON DC 20305		BALLISTIC MISSILE DEFENSE OFFICE	
		THE PENTAGON	
		WASHINGTON DC 20350	

DISTRIBUTION (Continued)

	<u>Copies</u>		<u>Copies</u>
ATTN SFAE SD ASP	1	NON-DOD ACTIVITIES	
SFAE SD HED	1	ATTN NEIL WALKER	1
DEPUTY COMMANDER		NICHOLAS RESEARCH CORPORATION	
US ARMY STRATEGIC DEFENSE COMMAND		MS 912	
P O BOX 1500		P O BOX 400002	
HUNTSVILLE AL 35807-3801		4040 S MEMORIAL PKWY	
		HUNTSVILLE AL 35801	
ATTN D WASHINGTON	1	THE CNA CORPORATION	
W WALKER	1	P O BOX 16268	
R KRETZSCHMAR	1	ALEXANDRIA VA 22302-0268	1
COMMAND GENERAL		ATTN GIFT AND EXCHANGE DIVISION	4
US ARMY MISSILE COMMAND		LIBRARY OF CONGRESS	
AMSMI-RD-SS-AT		WASHINGTON DC 20540	
REDSTONE ARSENAL AL 35898-5252		GIDEP OPERATIONS OFFICE	
DEFENSE TECHNICAL INFORMATION		CORONA CA 91720	1
CENTER		ATTN TECHNICAL LIBRARY	1
8725 JOHN J KINGMAN ROAD		NASA AMES RESEARCH CENTER	
SUITE 0944		MOFFETT CA 94035-1099	
FORT BELVOIR VA 22060-6218	12	ATTN C SCOTT	1
DIRECTOR		D CURRY	1
DEFENSE PRINTING SERVICE		NASA JOHNSON SPACE CENTER	
BLDG 176 WASHINGTON NAVY YARD		HOUSTON TX 77058	
901 M ST E		ATTN TECHNICAL LIBRARY	1
WASHINGTON DC 20374-5087	1	NASA	
ATTN CODE E29L		WASHINGTON DC 20546	
TECHNICAL LIBRARY	1	ATTN W C SAWYER	1
COMMANDING OFFICER		B HENDERSON	1
COASTAL SYSTEMS STATION		D MILLER	1
DAHLGREN DIVISION		J ALLEN	1
NAVAL SURFACE WARFARE CENTER		F WILCOX	1
6703 W HIGHWAY 98		TECHNICAL LIBRARY	2
PANAMA CITY FL 32407-7001		NASA LANGLEY RESEARCH CENTER	
ATTN DR P WEINACHT	1	HAMPTON VA 23365	
AERODYNAMICS BRANCH			
PROPULSION AND FLIGHT DIV WTD			
AMSRL WT PB			
US ARMY RESEARCH LAB ABERDEEN			
PROVING GROUND MD 21005-5066			

DISTRIBUTION (Continued)

	<u>Copies</u>		<u>Copies</u>
ATTN D G MILLER (L-219)	1	ATTN PROF J A SCHETZ	1
TECHNICAL LIBRARY	1	VIRGINIA POLYTECHNIC AND STATE	
LAWRENCE LIVERMORE NATIONAL		UNIVERSITY	
LABORATORY		DEPT OF AEROSPACE ENGINEERING	
EARTH SCIENCES DIVISION		BLACKSBURG VA 24060	
UNIVERSITY OF CALIFORNIA			
P O BOX 808		ATTN J M WU	1
LIVERMORE CA 94550		C BALASUBRAMAYAN	1
		TECHNICAL LIBRARY	1
ATTN W RUTLEDGE (1635)	1	THE UNIVERSITY OF TENNESSEE	
R LAFARGE	1	SPACE INSTITUTE	
R EISLER	1	TULLAHOMA TN 37388	
TECHNICAL LIBRARY	1		
SANDIA NATIONAL LABORATORY		ATTN R NELSON	1
P O BOX 5800		TECHNICAL LIBRARY	1
ALBUQUERQUE NM 87185-5800		UNIVERSITY OF NOTRE DAME	
		DEPT OF AEROSPACE AND	
ATTN ASSISTANT DEFENSE		MECHANICAL ENGINEERING	
COOPERATION ATTACHE	1	BOX 537	
EMBASSY OF SPAIN		NOTRE DAME IN 46556	
WASHINGTON DC 20016			
ATTN CDR R TEMPEST	1	ATTN PROF F NELSON	1
BRITISH NAVY STAFF		DEPT OF MECH AND AERO ENG	
WASHINGTON DC 20008		UNIVERSITY OF MISSOURI ROLLA	
		ROLLA MO 65401	
ATTN ASO LO IS	1	ATTN DR DONALD SPRING	1
ISRAEL AIR FORCE		AEROSPACE ENGINEERING DEPT	
LIAISON OFFICER		AUBURN UNIVERSITY AL 36849-5338	
700 ROBBINS AVE			
PHILADELPHIA PA 19111		ATTN ROBERT ENGLAR	1
		GEORGIA TECH RESEARCH INSTITUTE	
ATTN GERMAN MILITARY REP US OA	1	AEROSPACE SCIENCE AND	
GMR TRAFFIC AND TRANSPORTATION		TECHNOLOGY LAB	
DIVISION		ATLANTA GA 30332	
10 SERVICES ROAD			
DULLES INTERNATIONAL AP		ATTN E LUCERO	1
WASHINGTON DC 20041		L TISSERAND	1
		D FROSTBUTTER	1
ATTN F D DEJARNETTE	1	L PERINI	1
NORTH CAROLINA STATE UNIVERSITY		TECHNICAL LIBRARY	1
DEPT OF MECHANICAL AND		APPLIED PHYSICS LABORATORY	
AEROSPACE ENGINEERING		JOHNS HOPKINS UNIVERSITY	
BOX 7921		JOHNS HOPKINS ROAD	
RALEIGH NC 27695		LAUREL MD 20723-6099	

DISTRIBUTION (Continued)

	<u>Copies</u>		<u>Copies</u>
ATTN B BROOKS	1	ATTN J WILLIAMS	1
R STANCIL	1	S VUKELICH	1
R ELKINS	1	J FIVEL	1
LORAL VOUGHT SYSTEMS		R GERBSCH (CODE 1111041)	1
P O BOX 650003		TECHNICAL LIBRARY	1
M S EM 55		MCDONNELL DOUGLAS	
DALLAS TX 75265-0003		ASTRONAUTICS CO (EAST)	
		BOX 516	
ATTN TECHNICAL LIBRARY	1	ST LOUIS MO 63166-0516	
MARTIN MARIETTA AEROSPACE			
P O BOX 5837		ATTN TECHNICAL LIBRARY	1
ORLANDO FL 32805		UNITED TECHNOLOGIES	
		NORDEN SYSTEMS	
ATTN R CAVAGE	1	NORWALK CT 06856	
ADVANCED SYSTEMS DESIGN			
DEPT 113 407 (GB14)		ATTN T LUNDY	1
ROCKWELL		D ANDREWS	1
NORTH AMERICAN AIRCRAFT		TECHNICAL LIBRARY	1
OPERATIONS		LOCKHEED MISSILES AND	
P O BOX 92098		SPACE CO INC	
LOS ANGELES CA 90009		P O BOX 1103	
		HUNTSVILLE AL 35807	
ATTN TECHNICAL LIBRARY	1		
HUGHES MISSILE SYSTEMS COMPANY		ATTN W CHRISTENSON	1
P O BOX 11337 BLDG 802 MS A1		D WARNER	1
OLD NOGALES HWY		ALLIANT TECHSYSTEMS INC	
TUCSON AZ 83734-1337		600 SECOND ST NE	
		HOPKINS MN 55343	
ATTN M DILLENUS	1		
NIELSEN ENGINEERING AND		ATTN TECHNICAL LIBRARY	1
RESEARCH INC		B SALAMI	1
526 CLYDE AVE		J BOUDREAU	1
MOUNTAIN VIEW CA 95043		RAYTHEON COMPANY	
		MISSILE SYSTEMS DIVISION	
ATTN J XERIKOS	1	P O BOX 1201	
N CAMPBELL	1	TEWKSBURY MA 01876-0901	
TECHNICAL LIBRARY	1		
MCDONNELL DOUGLAS		ATTN LLOYD PRATT	1
ASTRONAUTICS CO (WEST)		AEROJET TACTICAL SYSTEMS CO	
5301 BOLSA AVE		P O BOX 13400	
HUNTINGTON BEACH CA 92647		SACRAMENTO CA 95813	
		ATTN JOWEPH ANDRZIJEWski	1
		MEVATEC CORP	
		1525 PERIMETER PARKWAY	
		SUITE 500	
		HUNTSVILLE AL 35806	

DISTRIBUTION (Continued)

	<u>Copies</u>		<u>Copies</u>
ATTN DR G S SCHMIDT LORAL DEFENSE SYSTEMS 1210 MASSILLAN ROAD AKRON OH 44315-0001	1	ATTN J FORKOIS KAMAN SCIENCES CORP 1500 GARDEN OF THE GODS ROAD P O BOX 7463 COLORADO SPRINGS CO 80933	1
ATTN W NORDGREN 721 GOULD INC OSD 18901 EUCLID AVE CLEVELAND OH 44117	1	ATTN FRED KAUTZ MIT LINCOLN LABORATORY LEXINGTON MA 02173-0073	1
ATTN TECH LIBRARY AEROJET ELECTRONIC SYSTEMS P O BOX 296 III AZUSA CA 91702	1	ATTN D J GRIESE MAIL STOP 4C 61 BOEING DEFENSE AND SPACE GROUP P O BOX 3999 SEATTLE WA 98124-2499	1
ATTN L E ERICSSON P REDING G CHRUSCIEL TECHNICAL LIBRARY LOCKHEED MISSILES AND SPACE CO INC P O BOX 504 SUNNYVALE CA 94086	1 1 1 1	ATTN W J CLARK DYNA EAST CORPORATION 3132 MARKET ST PHILADELPHIA PA 19104	1
ATTN K C LEE ACCUREX CORP P O BOX 7040 520 CLYDE AVE MOUNTAIN VIEW CA 94039	1	ATTN BRIAN WALKUP HERCULES AEROSPACE PRODUCT CO ALLEGHANY BALLISTIC LAB ROCKET CENTER WV 26726	1
ATTN TECH LIBRARY FMC NAVAL SYSTEMS DIV 4800 E RIVER ROAD MINNEAPOLIS MN 55421-1402	1	ATTN B D PRATS MARTIN MARIETTA ASTROSPACE AEROTHERMOPHYSICS 230 E GODDARD BLVD KING OF PRUSSIA PA 19406	1
ATTN DORIA GLADSTONE BATTELLE MEMORIAL INSTITUTE COLUMBUS DIVISION 505 KING AVE COLUMBUS OH 43201-2693	1	ATTN DR T LIN TRW ELECTRONICS AND DEFENSE SECTOR BLDG 527/RM 706 P O BOX 1310 SAN BERNADINO CA 92402	1
ATTN JAMES SORENSON ORBITAL SCIENCES 3380 SOUTH PRICE ROAD CHANDLER AZ 85248	1	ATTN G VINCENT SPARTA INC 4301 CORPORATE DR HUNTSVILLE AL 35805	1

DISTRIBUTION (Continued)

	<u>Copies</u>		<u>Copies</u>
ATTN D P FORSMO	1	ATTN WILLIAM FACINELLI	1
TECHNICAL LIBRARY	1	ALLIED SIGNAL	
RAYTHEON COMPANY		P O BOX 22200	
MISSILE SYSTEMS DIVISION		MS 1230 21E	
HARTWELL RD		TEMPE AZ 85285	
BEDFORD MA 01730-2498			
ATTN M S MILLER	1	ATTN DR T P SHIVANANDA	1
BRIAN EST	1	TRW BMD	
DYNETICS INC		P O BOX 1310	
P O DRAWER B		SAN BERNADINO CA 92402-1313	
HUNTSVILLE AL 35814-5050			
ATTN H A MCELROY	1	ATTN T R PEPITONE	1
GENERAL DEFENSE CORP		AEROSPACE TECHNOLOGY INC	
P O BOX 127		P O BOX 1809	
RED LION PA 17356		DAHLGREN VA 22448	
ATTN R SEPLAK	1	ATTN ERIC MOORE	1
BRUNSWICK CORP		MAIL STOP MER 24 1281	
DEFENSE DIVISION		LOCKHEED SANDERS	
3333 HARBOR BLVD		P O BOX 868	
COSTA MESA CA 92628-2009		NASHUA NH 03061	
ATTN J W MCDONALD	1	ATTN DR BRIAN LANDRUM	
GENERAL RESEARCH CORP		RI BLDG E33	1
ADVANCED TECHNOLOGY INC		PROPULSION RESEARCH CENTER	
5383 HOLLISTER AVE		UNIVERSITY OF ALABAMA	
P O BOX 6770		HUNTSVILLE AL 35899	
SANTA BARBARA CA 93160-6770		ATTN BRUCE NORTON	
ATTN CAROL BUTLER	1	MAIL STOP BL 1	1
OTI INTERNATIONAL		RAYTHEON	
60 2ND ST SUITE 301		100 VANCE TANK RD	
P O BOX 37		BRISTOL TN 37620	
SHALIMAR FL 32579		ATTN JIM ROBERTSON	1
ATTN ENGINEERING LIBRARY	1	RESEARCH SOUTH INC	
ARMAMENT SYSTEMS DEPT		555 SPARKMAN DRIVE	
GENERAL ELECTRIC CO		SUITE 818	
BURLINGTON VT 05401		HUNTSVILLE AL 35816-3423	
ATTN TECHNICAL LIBRARY	1	ATTN BOB WHYTE	1
OAYNE AERONAUTICAL		ARROW TECH ASSOCIATES INC	
2701 HARBOR DRIVE		1233 SHELBURNE ROAD D8	
SAN DIEGO CA 92138		SO BURLINGTON VT 05403	

DISTRIBUTION (Continued)

	<u>Copies</u>		<u>Copies</u>
ATTN JUAN AMENABAR SAIC 1700 N MOORE ST STE 1820 ARLINGTON VA 22209	1	ATTN MAJ F DE COCK ECOLE ROYALE MILITAIRE 30 AV DE LA RENAISSANCE 1040 BRUXELLES BELGIUM	1
ATTN TECHNICAL LIBRARY TELEDYNE RYAN AERONAUTICAL 2701 HARBOR DRIVE SAN DIEGO CA 92138	1	ATTN J EKEROOT BOFORS MISSILES 691 80 KARLSKOGA SWEDEN	1
NON-DOD ACTIVITIES (EX-CONUS)			
ATTN LOUIS CHAN INSTITUTE FOR AEROSPACE RESEARCH NATIONAL RESEARCH COUNCIL MONTREAL RD OTTAWA ONTARIO CANADA K1A0R6	1	ATTN CH FRANSSON NATIONAL DEFENCE RESEARCH ESTABLISHMENT DEPT OF WEAPON SYSTEMS EFFECTS AND PROTECTION KARLAVAGEN 106B 172 90 SUNDBYBERG SWEDEN	1
ATTN H B ASLUND SAAB MILITARY AIRCRAFT 581 88 LINKOEPING SWEDEN	1	ATTN M HARPER-BOURNE DEFENCE RESEARCH AGENCY Q134 BUILDING RAE FARNBOROUGH HAMPSHIRE QU14 6TD UNITED KINGDOM	1
ATTN R BARDWELL DEFENSE SYSTEMS LTD THE GROVE, WARREN LANE STANMORE, MIDDLESEX UNITED KINGDOM	1	ATTN A H HASSELROT FFA P O BOX 11021 161 11 BROMMA SWEDEN	1
ATTN A BOOTH BRITISH AEROSPACE DEFENCE LTD MILITARY AIRCRAFT DIVISION, WARTON AERODROME WARTON PRESTON, LANCASHIRE PR4 1AX UNITED KINGDOM	1	ATTN B JONSSON DEFENCE MATERIAL ADMINISTRATION MISSILE TECHNOLOGY DIVISION 115 88 STOCKHOLM SWEDEN	1
ATTN R CAYZAC GIAT INDUSTRIES 7 ROUTE DE GUERCY 18023 BOURGES CEDEX FRANCE	1	ATTN P LEZEAUD DASSAULT AVIATION 78 QUAI MARCEL DASSAULT 92214 SAINT-CLOUD FRANCE	1

DISTRIBUTION (Continued)

	<u>Copies</u>		<u>Copies</u>
ATTN J LINDHOUT N L R ANTHONY FOKKERWEG 2 1059 CM AMSTERDAM THE NETHERLANDS	1	ATTN J SOWA SAAB MISSILES AB 581 88 LINKOPING SWEDEN	1
ATTN A MICKELLIDES GEC MARCONI DEFENCE SYSTEMS LTD THE GROVE WARREN LANE STANMORE MIDDLESEX UNITED KINGDOM	1	ATTN D SPARROW HUNTING ENGINEERING LTD REDDINGS WOOD AMPTHILL BEDFORDSHIRE MK452HD UNITED KINGDOM	1
ATTN K MOELLER BODENSEEWERK GERAETETECHNIK GMBH POSTFACH 10 11 55 88641 UBERLINGEN GERMANY	1	ATTN P STUDER DEFENCE TECHNOLOGY AND PROCUREMENT AGENCY SYSTEMS ANALYSIS AND INFORMATION SYSTEMS DIVISION PAPIERMUEHLESTRASSE 25 3003 BERNE SWITZERLAND	1
ATTN G MOSS ROYAL MILITARY COLLEGE AEROMECHANICAL SYSTEMS GROUP SHRIVENHAM SWINDON WILTS SN6 8LA UNITED KINGDOM	1	ATTN DR R G LACAU AEROSPATIALE - MISSILE DEPT E/ECN CENTRE DES GATINES 91370 VERRIERE LE BUISSON FRANCE	1
ATTN RIBADEAU DUMAS MATRA DEFENSE 37 AV LOUIS BREGUET BP 1 78146 VELIZY-VILLACOUBLAY CEDEX FRANCE	1	ATTN J M CHARBONNIER VON KARMAN INSTITUTE 72 CHAUSSEE DE WATERLOO 1640 RHODE-SAINT-GENESE BELGIUM	1
ATTN R ROGERS DEFENCE RESEARCH AGENCY BLDG 37 TUNNEL SITE CLAPHAM BEDS MK 41 6AE UNITED KINGDOM	1	ATTN P CHAMPIGNY DIRECTION DE L'AERONAUTIQUE ONERA 29 AV DE LA DIVISION LECLERC 92320 CHATILLON-SOUS-BAGNEUX CEDEX FRANCE	1
ATTN S SMITH DEFENCE RESEARCH AGENCY Q134 BUILDING RAE FARNBOROUGH HAMPSHIRE QU14 6TD UNITED KINGDOM	1	ATTN DR P HENNIG DEUTSCHE AEROSPACE (DASA) VAS 414 ABWEHR AND SCHUTZ POSTFACH 801149 8000 MUENCHEN 80 GERMANY	1

DISTRIBUTION (Continued)

	<u>Copies</u>		<u>Copies</u>
ATTN H G KNOCHE	1	K204	1
DR GREGORIOU	1	N	1
MESSERSCHMIDT BOLKOW BLOHM			
GMBH			
UNTERNEHMENSBEREICH APPARATAE			
MUNCHEN 80 POSTFACH 801149 BAYERN			
GERMANY			
 INTERNAL			
A	1		
B	1		
B05 (STATON)	1		
B44	1		
B44 (PRIOLO)	1		
B44 (HSIEH)	1		
B44 (WARDLAW)	1		
B51 (ARMISTEAD)	1		
B60 (LIBRARY)	3		
C	1		
D	1		
D4	1		
F	1		
G	1		
G02	1		
G04	5		
G20	1		
G205	1		
G23	1		
G23 (CHADWICK)	1		
G23 (GRAFF)	1		
G23 (HARDY)	1		
G23 (HYMER)	5		
G23 (MCINVILLE)	5		
G23 (OHLMEYER)	1		
G23 (ROWLES)	1		
G23 (WEISEL)	1		
G30	1		
G305	1		
G40	1		
G50	1		
G60	1		
G70	1		
G72	1		
K	1		
K10	1		
K20	1		